

Mathematical Models and Methods in Applied Sciences
 © World Scientific Publishing Company

Fourth- and Higher-order Interface Tracking of Three or More Materials with Arbitrarily Complex Topology and Geometry*

Yan Tan, Yixiao Qian[†], Zhiqi Li

*School of Mathematical Sciences, Zhejiang University
 Hangzhou, Zhejiang 310058, China
 yantanhn@zju.edu.cn
 yixiaoqian@zju.edu.cn
 li-zhiqi@zju.edu.cn*

Qinghai Zhang[‡]

*School of Mathematical Sciences, Zhejiang University
 Hangzhou, Zhejiang 310058, China*

*Institute of Fundamental and Transdisciplinary Research, Zhejiang University
 Hangzhou, Zhejiang 310058, China
 qinghai@zju.edu.cn*

Received (Day Month Year)

Revised (Day Month Year)

Communicated by (xxxxxxxxxx)

For interface tracking of an arbitrary number of materials in two dimensions, we propose a multiphase cubic MARS method that (a) accurately and efficiently represents the topology and geometry of the interface via graphs, cycles, and cubic splines, (b) maintains a (r, h) -regularity condition of the interface so that the distance between any pair of adjacent markers is within a user-specified range that may vary according to the local curvature, (c) applies to multiple materials with arbitrarily complex topology and geometry, and (d) achieves fourth-, sixth-, and eighth-order accuracy both in time and in space. In particular, all possible types of junctions, which pose challenges to VOF methods and level-set methods, are handled with ease. The fourth- and higher-order convergence rates of the proposed method are proven under the MARS framework. Results of classic benchmark tests confirm the analysis and demonstrate the superior accuracy and efficiency of the proposed method.

Keywords: Multiphase and multicomponent flows; moving boundary problems; interface tracking (IT); Yin sets; mapping and adjusting regular semianalytic sets (MARS)

76T30, 65D07, 05C90

***Funding:** This work was supported by grants #12272346 and #11871429 from the National Natural Science Foundation of China.

[†]Yan Tan and Yixiao Qian contributed equally to this work and are co-first authors.

[‡]Corresponding author

1. Introduction

As a complex yet significant topic, multiphase flows concern the simultaneous movements and interactions of a number of homogeneous *materials* or *phases* such as liquids, gases, and solids. These flows are prevalent in natural and industrial processes yet pose major challenges to high-fidelity simulations in applied sciences. One fundamental problem that accounts for these challenges is interface tracking (IT), the determination of regions occupied by these phases.

The most popular families of IT methods are probably level-set methods, front-tracking methods, and volume-of-fluid (VOF) methods. In level-set methods, the interface is *implicitly* approximated as the zero isocontour of a signed distance function while, in front-tracking methods, it is *explicitly* represented as a set of connected markers. In VOF methods, the interface is not only implicitly described by volume fractions of the tracked phase inside fixed control volumes but also explicitly represented as a cellwise function. Within each time step, a VOF method consists of two substeps: in the first reconstruction substep the explicit representation of material regions is determined *solely* from volume fractions while in the second advection substep the volume fractions are advanced to the end of the time step from the explicit representation and the velocity field.

In the last half-century, many IT methods have been developed for two-phase flows, where it is sufficient to track only one phase and deduce the region of the other. Most of the state-of-the-art IT methods are second-order accurate for two-phase flows. The cubic MARS method,²⁶ which belong to none of the aforementioned three families, even achieve fourth- and higher-order accuracy.

In contrast, for IT of three or more phases, the literature is much thinner and the accuracy of current IT methods is much lower; this case is referred to as the *multiphase IT problem* or the *IT problem of multiple materials* since more than one phase has to be tracked. The core difficulty in tracking multiple phases, however, lies not in the number of phases but in the topology and the geometry that are fundamentally more complicated than that of two-phase flows. For example, an interface curve might have a *kink*, i.e., a C^1 discontinuity of the curve function as in Definition 4.6, which is problematic for level-set methods and VOF methods: large reconstruction errors at these kinks are propagated along the interface in subsequent time steps by numerical diffusion, altering geometric features of sharp corners to rounded shapes. As another example, three or more phases might meet at a *junction* (see Definition 4.5), where the boundary curve of at least one phase contains kinks. These kinks cause more damage to the fidelity of simulating multiple phases than two-phase flows because of (i) the large slope change of a boundary curve at the junction, and more importantly, (ii) junctions usually being the places of our primary interests where important physics occur, e.g., the triple points of air-water-solid systems such as contact lines.^{21,30}

The standard level-set construction is not applicable to the local neighborhood of a junction because the zero level set of a single signed distance function is never

homeomorphic to the one-dimensional CW complex that characterizes the topology at the junction. To resolve this difficulty, Saye and Sethian¹⁸ propose the Voronoi implicit interface method as a generalization of the level set method for computing multiphase physics, via an elegant extension of the Voronoi diagram to a set of curves and surfaces. It is also the Voronoi diagram that determines the interface and consequently limits this method to first-order accuracy at the junctions.

The extension of VOF methods to multiple phases has been primarily focused on the reconstruction substep.⁴ Piecewise linear VOF reconstruction schemes for junctions are limited to triple points^{6,7} and it appears that no VOF schemes handle junctions with four or more incident edges. In the “onion-skin” model, the multiple materials inside a control volume are assumed to have a layered topology *with no junctions*. Given a material ordering, the interface between the i th and the $(i+1)$ th phases is defined by applying a VOF reconstruction scheme to the mixture of materials 1 through i . When two such reconstructed interfaces intersect, one either adjusts the interfaces to eliminate the intersection^{8,20} or scales the fluxes to account for volumes of overlapping areas [2, p. 365]. Consequently, the IT results depend substantially on the material ordering. Youngs²⁴ requires the user to specify a priority list, which implies a *static* material ordering for each cell. Mosso and Clancy¹⁶ propose to order the materials *dynamically* based on estimates of their centroids in each cell. Benson³ adds the estimated centroids as solution variables and determines the dynamic ordering by a least-squares fitting of a line to the centroids and then sorting the projected images of centroids along the line.

For material-order-dependent VOF methods, an incorrect ordering results in large errors in reconstruction and premature/belated advection of multiple phases.¹⁵ In addition, the topology of a junction might be changed by the numerical diffusion in these methods; see, e.g., the erroneous alteration of an X junction to two T junctions illustrated in [19, Fig. 16]. To alleviate these adverse effects, Schofield et al.¹⁹ develop a power diagram method, a material-order-independent interface reconstruction technique, in which the interface is first reconstructed by a weighted Voronoi diagram from material locator points and then improved by minimizing an objective function that smooths the interface normals.

Another extension of VOF methods is the moment-of-fluid (MOF) method,¹¹ which reconstructs cellwise materials not only by volume fractions (their 0th moments) but also by centroids (their 1st moments). Since these two moments already provide enough information to construct a linear function, no data from neighboring cells are needed. This independence furnishes a straightforward generalization from two phases to N_p phases, via enumerating all $N_p!$ possible orderings to minimize the error norm of the first moment. Despite being material-order-dependent, the MOF method is second-order accurate if the true interface is \mathcal{C}^2 -serial, i.e., if all phases can be sequentially separated from the bulk by \mathcal{C}^2 curves.¹¹ For example, the interface in Fig. 1(a) is \mathcal{C}^2 -serial at the T junctions on the ellipse, but not so at the Y junction inside the ellipse, where the MOF reconstruction is only first-order accurate. See¹⁵ for an accuracy comparison of MOF and VOF methods.

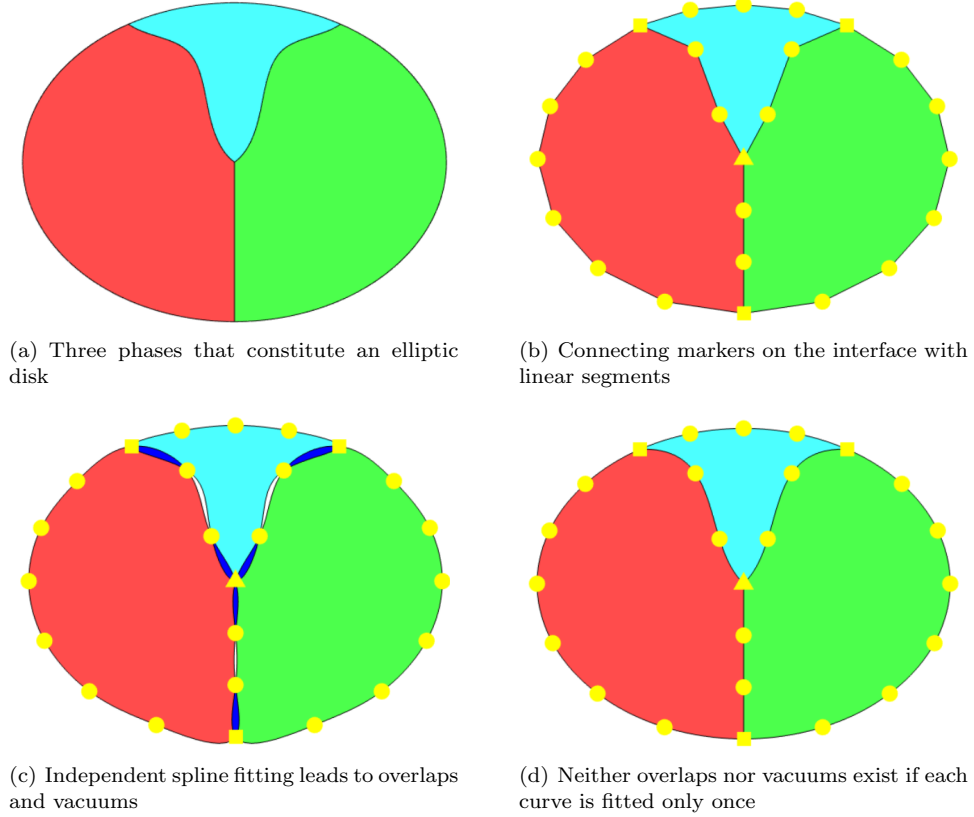
4 *Y. Tan & Y. Qian & Z. Li & Q. Zhang*

Fig. 1. Boundary representations of multiple phases. Subplot (a) shows three phases to be represented by a set of interface markers or characteristic points (squares, triangles, and dots). In subplot (b), the markers are connected by linear segments, yielding a second-order representation without creating overlaps and vacuums between adjacent phases. In subplot (c), fitting \mathcal{C}^2 periodic cubic splines independently for each phase leads to overlaps (blue areas) and vacuums (white areas inside the ellipse). At each of the *T junctions* (squares), there exist two curve segments forming a smooth curve whereas, at the *Y junction* (the triangle), all curves formed by connecting two radial curve segments can only be \mathcal{C}^0 . Therefore, in subplot (d), the smooth ellipse is represented by a \mathcal{C}^2 periodic cubic spline while the three radial curve segments incident to the Y-junction are approximated separately by not-a-knot cubic splines; see Definition 4.11.

Interestingly, multiphase MOF reconstruction is helpful for two-phase flows in capturing filaments, thin strands of one material surrounded by another within a cell, e.g., the tail tips in Fig. 6(h,k). Jemison et al.¹⁴ introduce a fictitious phase to reformulate the filament reconstruction as three materials separated by two interfaces in an onion-skin topology. Hergibo et al.¹² resolve filaments via a symmetric multi-material approach with accurate routines from computational geometry such as polygon clipping. These multiphase MOF methods reconstruct filaments more accurately than the standard MOF for two phases; see Table 2(b,c).

As far as we know, neither level-set methods nor VOF/MOF methods are capable of reconstructing *all* types of junctions to second-order accuracy; in particular, they all drop to first-order accuracy at Y junctions. A front tracking method, with the aid of graphs such as that in Definition 4.7, can represent the interface topology exactly and thus achieves full second-order accuracy, so long as all junctions and kinks are already selected as interface markers. In particular, such a front-tracking method is independent of material ordering. Even if interface markers are tracked twice, neither overlaps nor vacuums are created between adjacent phases provided that the markers are connected with *linear* segments; see Fig. 1(b). However, this statement does not hold for higher-order splines: to achieve an accuracy higher than the second order, one needs the geometric information at each junction on the pairing of smoothly connected curve segments. As shown in Fig. 1(c), independent approximations of the boundary Jordan curve of each phase with \mathcal{C}^2 periodic cubic splines result in overlaps and vacuums between adjacent phases. In contrast, a blend of periodic and not-a-knot cubic splines fitted with due considerations of topological structures and geometric features give satisfactory results; see Fig. 1(d).

For traditional IT methods, why is it so difficult to achieve high-order accuracy for multiple materials? In our humble opinion, the reason is that *topology and geometry are avoided in these methods via converting topological and geometric problems in IT to numerically differential equations*, such as the ordinary differential equations (ODEs) of interface markers in front-tracking methods or scalar conservation laws in level-set and VOF methods. Being relinquished at the very beginning, key topological structures and geometric features can hardly be recovered to high-order accuracy in subsequent time steps. Indeed, the MOF methods^{11,12,14} are still at best second-order accurate, even after utilizing more geometric information. For front-tracking methods, the connected markers need to be supplemented with additional information on the topology and geometry of the multiple phases; otherwise the accuracy can not be higher than the second order.

The above discussions motivate questions as follows.

- (Q-1) Given their physical significance, can kinks and junctions of all possible types be faithfully represented and accurately tracked without creating overlaps and vacuums between adjacent phases?
- (Q-2) VOF and level-set methods cannot preserve geometric features under isometric flow maps, nor can they preserve topological structures under homeomorphic flow maps. To resolve these difficulties, can we develop an IT method that preserves topological structures and geometric features for multiple materials under homeomorphic flow maps?
- (Q-3) For large geometric deformations, can we maintain some regularity on the marker sequence so that spline interpolations of the interface are guaranteed to be sufficiently accurate and well conditioned?
- (Q-4) Can we design an efficient IT method that is fourth- and higher-order accurate for tracking multiple phases with arbitrarily complex topology and geometry?

(Q-5) Can we prove the adjacency-preserving feature in (Q-1) and the high-order convergence rates in (Q-4)?

In this paper, we provide positive answers to all above questions. Fundamentally different from that of current IT methods, our primary principle is to *tackle topological and geometric problems in IT with tools in topology and geometry*.

Previously, we have proposed a topological space (called the Yin space) as a mathematical model of two-dimensional continua,²⁸ analyzed explicit IT methods under the framework of mapping and adjusting regular semianalytic sets (MARS),²⁷ developed a cubic MARS method for two-phase flows,²⁶ and augmented MARS methods to curve shortening flows via the strategy of adding and removing markers (ARMS).¹³ As an extension of MARS to multiple materials, this work is another manifestation that IT methods coupling (even elementary) concepts in topology and geometry can be highly accurate and highly efficient.

The main contributions of this work are

- the mathematical models and data structures for representing topological structures and geometric features of multiple materials with arbitrary complexity,
- a multiphase cubic MARS method for solving the multiphase IT problem in Section 3,
- a rigorous proof of the fourth- and higher-order convergence rates of the proposed multiphase MARS method.

The rest of this paper is structured as follows. Section 2 is a brief review on the Yin space, with all interface topology classified in Theorem 2.2. Section 3 is a precise definition of the multiphase IT problem. In Section 4, we answer (Q-1,2) by designing concepts and data structures for representing *static* multiple phases and by separating their topology from the geometry. In particular, the accuracy of periodic splines and not-a-knot splines in respectively approximating closed curves and curve segments is examined to prepare for the full analysis in Section 6. In Section 5, we resolve (Q-3) by adapting the ARMS strategy¹³ to ensure the (r_{tiny}, h_L) -regularity condition in Definition 4.13. Then we propose in Definition 5.7 the cubic MARS method for multiple phases as our answer to (Q-4). In Section 6, we answer (Q-5) by proving the high-order convergence rates of the proposed method under the MARS framework. In Section 7, we demonstrate the fourth-, sixth-, and eighth-order accuracy of the proposed MARS method by results of classic benchmark tests. Finally, we conclude this paper in Section 8 with several future research prospects.

2. Modeling continua by Yin sets

In a topological space \mathcal{X} , the *complement* of a subset $\mathcal{P} \subseteq \mathcal{X}$, written \mathcal{P}' , is the set $\mathcal{X} \setminus \mathcal{P}$. The *closure* of a set $\mathcal{P} \subseteq \mathcal{X}$, written $\bar{\mathcal{P}}$, is the intersection of all closed supersets of \mathcal{P} . The *interior* of \mathcal{P} , written \mathcal{P}° , is the union of all open subsets of \mathcal{P} .

The *exterior* of \mathcal{P} , written $\mathcal{P}^\perp := \mathcal{P}'^\circ := (\mathcal{P}')^\circ$, is the interior of its complement. A point $\mathbf{x} \in \mathcal{X}$ is a *boundary point* of \mathcal{P} if $\mathbf{x} \notin \mathcal{P}^\circ$ and $\mathbf{x} \notin \mathcal{P}^\perp$. The *boundary* of \mathcal{P} , written $\partial\mathcal{P}$, is the set of all boundary points of \mathcal{P} . It can be shown that $\mathcal{P}^\circ = \mathcal{P} \setminus \partial\mathcal{P}$ and $\overline{\mathcal{P}} = \mathcal{P} \cup \partial\mathcal{P}$.

A *regular open* set is an open set \mathcal{P} satisfying $\mathcal{P} = \overline{\mathcal{P}}^\circ$ while a *regular closed* set is a closed set \mathcal{P} satisfying $\mathcal{P} = \overline{\mathcal{P}^\circ}$. Regular sets, open or closed, capture a key feature of continua that their regions are free of lower-dimensional elements such as isolated points and curves in \mathbb{R}^2 and dangling faces in \mathbb{R}^3 . The intersection of two regular sets, however, might contain an infinite number of connected components [28, eqn (3.1)], making it difficult to perform Boolean algorithms on regular sets since no computer has an infinite amount of memory. This difficulty is resolved by requiring each regular set to be simultaneously a *semianalytic* set, i.e., a set $\mathcal{S} \subseteq \mathbb{R}^D$ in the universe of a finite Boolean algebra formed from the sets $\mathcal{X}_i = \{\mathbf{x} \in \mathbb{R}^D : g_i(\mathbf{x}) \geq 0\}$ where each $g_i : \mathbb{R}^D \rightarrow \mathbb{R}$ is an analytic function. Intuitively, $\partial\mathcal{S}$ is piecewise \mathcal{C}^∞ so that \mathcal{S} can be described by a finite number of entities.

Definition 2.1 (Yin space^{27,28}). A *Yin set* $\mathcal{Y} \subseteq \mathbb{R}^D$ is a regular open semianalytic set whose boundary is bounded. All Yin sets form the *Yin space* \mathbb{Y} .

A *curve (segment)* is (the image of) a continuous map $\gamma : [0, 1] \rightarrow \mathbb{R}^2$; it is *closed* if its *endpoints* coincide, i.e., $\gamma(0) = \gamma(1)$. The *open curve* of a curve segment γ is its restriction $\gamma|_{(0,1)}$, whose endpoints are those of γ . An open curve is *simple* if it is injective. A curve is *Jordan* if it is closed and its corresponding open curve is simple. The *interior of an oriented Jordan curve*, written $\text{int}(\gamma)$, is the component of $\mathbb{R}^2 \setminus \gamma$ that always lies to the left of the observer who traverses γ according to $\gamma([0, 1])$. A Jordan curve γ is *counterclockwise* or *positively oriented* if $\text{int}(\gamma)$ is the bounded component of $\mathbb{R}^2 \setminus \gamma$; otherwise it is *clockwise* or *negatively oriented*.

Following [28, Def. 3.7], we call two Jordan curves *almost disjoint* if they have no proper intersections (i.e., crossings) and the number of their improper intersections is finite. A Jordan curve γ_k is said to *include* another Jordan curve γ_ℓ , written $\gamma_k \geq \gamma_\ell$ or $\gamma_\ell \leq \gamma_k$, if the bounded complement of γ_ℓ is a subset of that of γ_k . If γ_k includes γ_ℓ and $\gamma_k \neq \gamma_\ell$, we write $\gamma_k > \gamma_\ell$ or $\gamma_\ell < \gamma_k$. In a partially ordered set (poset) \mathcal{J} of Jordan curves with inclusion as the partial order, we say that γ_k *covers* γ_ℓ in \mathcal{J} and write ' $\gamma_k \succ \gamma_\ell$ ' or ' $\gamma_\ell \prec \gamma_k$ ' if $\gamma_\ell < \gamma_k$ and no element $\gamma \in \mathcal{J}$ satisfies $\gamma_\ell < \gamma < \gamma_k$.

In Definition 2.1, a regular open set instead of a regular closed set is employed because the former can be *uniquely* represented by its boundary Jordan curves while the latter cannot [28, Fig. 5].

Theorem 2.2 (Global topology and boundary representation of connected Yin sets²⁸). *The boundary of any connected Yin set $\mathcal{Y} \neq \emptyset, \mathbb{R}^2$ can be uniquely partitioned into a finite set of pairwise almost disjoint Jordan curves, which can be uniquely oriented to yield a unique representation of \mathcal{Y} as $\mathcal{Y} = \bigcap_{\gamma_j \in \mathcal{J}_{\partial\mathcal{Y}}} \text{int}(\gamma_j)$ where $\mathcal{J}_{\partial\mathcal{Y}}$, the set of oriented boundary Jordan curves of \mathcal{Y} , must be one of the two*

8 Y. Tan & Y. Qian & Z. Li & Q. Zhang

types,

$$\begin{cases} \mathcal{J}^- = \{\gamma_1^-, \gamma_2^-, \dots, \gamma_{n_-}^-\} & \text{where } n_- \geq 1, \\ \mathcal{J}^+ = \{\gamma^+, \gamma_1^-, \gamma_2^-, \dots, \gamma_{n_-}^-\} & \text{where } n_- \geq 0, \end{cases} \quad (2.1)$$

and all γ_j^- 's are negatively oriented, mutually incomparable with respect to inclusion. In the case of \mathcal{J}^+ , γ^+ covers γ_j^- , i.e., $\gamma_j^- \prec \gamma^+$ holds for each $j = 1, 2, \dots, n_-$.

A form \mathcal{J}^- or \mathcal{J}^+ implies that the connected Yin set \mathcal{Y} is unbounded or bounded, respectively. In Fig. 2(a), \mathcal{M}_6 is unbounded while all other connected Yin sets are bounded; $n_- = 2$ for $\mathcal{M}_{4,1}$ and \mathcal{M}_5 and $n_- = 0$ for $\mathcal{M}_1, \mathcal{M}_2, \mathcal{M}_3$, and $\mathcal{M}_{4,2}$.

Theorem 2.3 (Boolean algebra on the Yin space²⁸). *The universal algebra $\mathbb{Y} := (\mathbb{Y}, \cup^{\perp\perp}, \cap, \perp, \emptyset, \mathbb{R}^2)$ is a Boolean algebra, where the regularized union is given by $\mathcal{Y} \cup^{\perp\perp} \mathcal{M} := (\mathcal{Y} \cup \mathcal{M})^{\perp\perp}$ for all $\mathcal{Y}, \mathcal{M} \in \mathbb{Y}$.*

The uniqueness of the boundary representation of Yin sets in Theorem 2.2 implies that \mathbb{Y} and \mathbb{J} are *isomorphic*, written $\mathbb{Y} \cong \mathbb{J}$, where \mathbb{J} is the *Jordan space* of posets of oriented Jordan curves. This isomorphism is exploited in²⁸ to reduce the above Boolean algebra to calculating intersections of boundary Jordan curves.

3. The multiphase IT problem

For any given initial time t_0 and initial position $p_0 \in \mathbb{R}^D$, the ODE

$$\frac{d\mathbf{x}}{dt} = \mathbf{u}(\mathbf{x}, t) \quad (3.1)$$

admits a unique solution if the time-dependent velocity field $\mathbf{u}(\mathbf{x}, t)$ is continuous in time and Lipschitz continuous in space. This uniqueness gives rise to a flow map $\phi : \mathbb{R}^D \times \mathbb{R} \times \mathbb{R} \rightarrow \mathbb{R}^D$ that takes the initial position p_0 of a Lagrangian particle p , the initial time t_0 , and the time increment τ and returns $p(t_0 + \tau)$, the position of p at time $t_0 + \tau$:

$$\phi_{t_0}^\tau(p) := p(t_0 + \tau) = p(t_0) + \int_{t_0}^{t_0 + \tau} \mathbf{u}(p(t), t) dt, \quad (3.2)$$

The flow map also generalizes to arbitrary point sets in a straightforward way,

$$\phi_{t_0}^\tau(\mathcal{M}) = \{\phi_{t_0}^\tau(p) : p \in \mathcal{M}\}. \quad (3.3)$$

If we further restrict the above point set to a Yin set, then the flow map ϕ for given t_0 and τ can be considered as a unitary operation $\phi_{t_0}^\tau : \mathbb{Y} \rightarrow \mathbb{Y}$. It is not difficult [1, p. 6] to show

Lemma 3.1. *For fixed t_0 and τ , the flow map $\phi_{t_0}^\tau : \mathcal{X} \rightarrow \mathcal{Y}$ in (3.3) is a diffeomorphism, i.e., a \mathcal{C}^1 bijection whose inverse is also \mathcal{C}^1 .*

In the IT problem, we are usually given *a priori* a velocity field $\mathbf{u}(\mathbf{x}, t)$, by which each fluid phase is passively advected. It is via this action of flow maps upon the Yin space that we formulate

Definition 3.2 (Multiphase IT). Given a sequence $(\mathcal{M}_i(t_0) \in \mathbb{Y})_{i=1}^{N_p}$ of pairwise disjoint Yin sets at the initial time t_0 , the *multiphase IT problem* is to determine the sequence $(\mathcal{M}_i(t) \in \mathbb{Y})_{i=1}^{N_p}$ of Yin sets at $T > t_0$ from a one-parameter group of diffeomorphic flow maps $\phi_{t_0} : \mathbb{R}^D \times [t_0, T] \rightarrow \mathbb{R}^D$ that acts upon $(\mathcal{M}_i(t_0))_{i=1}^{N_p}$ by (3.3).

Definition 3.2 extends the IT problem for a single phase in [26, Def. 3.1]. This extension is theoretically trivial in that the exact flow map can be applied to the Yin sets in any order to produce the exact results of IT. Nonetheless, the challenges of this multiphase IT problem mostly lie in the computational aspects such as the simultaneous preservations of high-order accuracy, phase adjacency, topological structures, and geometric features.

The setup of the multiphase IT problem in Definition 3.2 does not allow topological changes, since they are precluded by the diffeomorphic flow map of a single ODE (3.1). Although in this work we confine ourselves to homeomorphic movements for each phase, the data structures in Sec. 4, the algorithms in Sec. 5, and the analysis in Sec. 6 lay a solid ground to tackle multiphase IT problem with topological changes.

To sum up, the method proposed in this paper preserves topological structures and geometric features in the case of homeomorphic flow maps and in a future paper we will build on this work to handle topological changes accurately and efficiently.

4. Boundary representation of static Yin sets

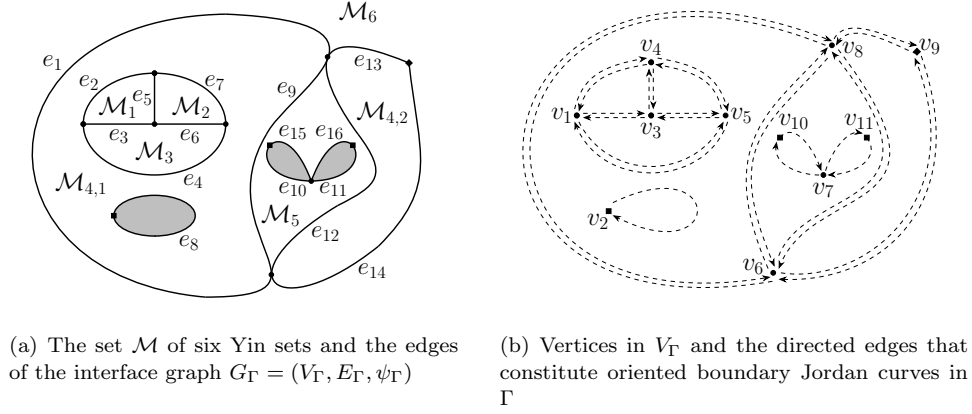
The N_p phases are identified with a set $\mathcal{M} := \{\mathcal{M}_i : i = 1, \dots, N_p\}$ of pairwise disjoint Yin sets, each of which is $\mathcal{M}_i := \bigcup_j^{\perp\perp} \mathcal{M}_{i,j}$ where $\mathcal{M}_{i,j}$ is the j th connected component of the i th phase \mathcal{M}_i . If \mathcal{M}_i is connected, we simply write \mathcal{M}_i for $\mathcal{M}_{i,1}$. Theorem 2.2 suggests

Notation 4.1. The (i, j) th *poset of oriented Jordan curves* of \mathcal{M} is denoted by $\Gamma_{i,j} := \{\gamma_{i,j}^k\}$ such that $\mathcal{M}_{i,j} = \bigcap_{\gamma_{i,j}^k \in \Gamma_{i,j}} \text{int}(\gamma_{i,j}^k)$. Denote by $N_{\mathcal{M}_i}$ the number of connected components of \mathcal{M}_i and we write

$$\begin{aligned} \Gamma_i &:= \{\Gamma_{i,j} : j = 1, \dots, N_{\mathcal{M}_i}\}, \quad \Gamma := \{\Gamma_i : i = 1, \dots, N_p\}; \\ \chi(\Gamma_{i,j}) &:= \bigcup_{\gamma_{i,j}^k \in \Gamma_{i,j}} \gamma_{i,j}^k, \quad \chi(\Gamma_i) := \bigcup_{j=1}^{N_{\mathcal{M}_i}} \chi(\Gamma_{i,j}), \quad \chi(\Gamma) := \bigcup_{i=1}^{N_p} \chi(\Gamma_i), \end{aligned} \quad (4.1)$$

where $\chi(\Gamma_{i,j})$ is a subset of \mathbb{R}^2 , so are $\chi(\Gamma_i) = \partial\mathcal{M}_i$ and the interface $\chi(\Gamma)$.

Due to the isomorphism $\mathbb{J} \cong \mathbb{Y}$, it suffices to represent $\mathcal{M}(t)$ by $\Gamma(t)$; the rule of thumb of our design is to *separate the topology of $\Gamma(t)$ from the geometry of $\Gamma(t)$* . Since the flow map in Definition 3.2 is a homeomorphism, only the *geometry* of $\Gamma(t)$

10 *Y. Tan & Y. Qian & Z. Li & Q. Zhang*


$\mathcal{M}_{i,j}$	$\gamma_{i,j}^k$	directed cycle $C_{i,j}^k$ of $\gamma_{i,j}^k$	smooth?	$\mathbf{e} \in C_S$	$\mathbf{e} \in T_S$
\mathcal{M}_1	γ_1^+	$e_2 \rightarrow e_3 \rightarrow e_5$	no	-	(e_5)
\mathcal{M}_2	γ_2^+	$e_5 \rightarrow e_6 \rightarrow e_7$	no	-	(e_5)
\mathcal{M}_3	γ_3^+	$e_3 \rightarrow e_4 \rightarrow e_6$	no	-	(e_3, e_6)
$\mathcal{M}_{4,1}$	$\gamma_{4,1}^+$	$e_1 \rightarrow e_9$ (counterclockwise)	yes	(e_1, e_9)	-
	$\gamma_{4,1}^{1-}$	$e_2 \rightarrow e_7 \rightarrow e_4$	yes	(e_2, e_7, e_4)	-
	$\gamma_{4,1}^{2-}$	e_8 (clockwise)	yes	(e_8)	-
$\mathcal{M}_{4,2}$	$\gamma_{4,2}^+$	$e_{13} \rightarrow e_{12} \rightarrow e_{14}$	no	-	(e_{13}, e_{12}, e_{14})
\mathcal{M}_5	γ_5^+	$e_9 \rightarrow e_{12}$ (counterclockwise)	no	-	-
	γ_5^{1-}	$e_{10} \rightarrow e_{15}$ (clockwise)	no	-	$(e_{15}, e_{10}, e_{11}, e_{16})$
	γ_5^{2-}	$e_{16} \rightarrow e_{11}$ (clockwise)	no	-	$(e_{15}, e_{10}, e_{11}, e_{16})$
\mathcal{M}_6	γ_6^{1-}	$e_1 \rightarrow e_{13} \rightarrow e_{14}$	no	-	-

(c) Representing oriented boundary Jordan curves of the seven connected Yin sets. The set C_S of circuits and the set T_S of trails are intended for spline fitting. A smooth Jordan curve such as $\gamma_{4,1}^k$ corresponds to a circuit in C_S . In the last column, a trail \mathbf{e} corresponds to a smooth curve segment γ that is approximated by a not-a-knot spline; γ may or may not be closed.

Fig. 2. The boundary representation of six pairwise disjoint Yin sets whose regularized union covers the plane except the shaded regions. All Yin sets are connected except that \mathcal{M}_4 has two components: $\mathcal{M}_4 = \mathcal{M}_{4,1} \cup^{\perp\perp} \mathcal{M}_{4,2}$. The interface $\chi(\Gamma)$ is represented by the graph $G_\Gamma = (V_\Gamma, E_\Gamma, \psi_\Gamma)$ in Definition 4.7 with $E_\Gamma = \{e_i : i = 1, \dots, 16\}$ shown in (a) and $V_\Gamma = \{v_i : i = 1, \dots, 11\}$ in (b). Solid dots, diamonds, and solid squares respectively denote junctions in Definition 4.5, kinks in Definition 4.6, and basepoints in Definition 4.7. In (c), oriented boundary Jordan curves in Notation 4.1 and corresponding directed cycles in Notation 4.8 are enumerated for each of the seven connected Yin sets. As an edge partition of E_Γ , the circuits in C_S and the trails in T_S correspond to smooth closed curves and smooth curve segments, respectively approximated by periodic splines and not-a-knot splines in S_{CT} , cf. Definition 4.25 and Algorithm 1.

needs to be updated at each time step since the topology of $\Gamma(t)$ can be determined from the initial condition $\Gamma(t_0)$ once and for all.

A comprehensive example is shown in Fig. 2 to illustrate, throughout this section, key points of our design.

First, the topology of Γ in the case of $N_p > 2$ is fundamentally more complicated

than that of $N_p = 2$ because the common boundary of any two connected Yin sets might not be a Jordan curve, due to the potential presence of T junctions such as v_1, v_3, v_4, v_5 in Fig. 2(b). Although X junctions such as v_7 in Fig. 2(b) may also show up in two-phase flows, they tend to appear more frequently in three or more phases, cf. v_6, v_8 in Fig. 2(b). In both cases, the degree of a junction can be any positive integer greater than two. These complications are handled in Sec. 4.1.

Second, boundary Jordan curves of adjacent Yin sets may have distinct geometric features. In Fig. 2, $\gamma_{4,1}^{1-} \cap \gamma_1^+ = e_2$, but $\gamma_{4,1}^{1-}$ is smooth while γ_1^+ is only \mathcal{C}^0 due to the junctions v_1, v_3, v_4 . As shown in Fig. 1, separate approximations of Jordan curves may lead to overlaps and/or vacuums of adjacent phases. This problem can be solved by approximating each common boundary *only once* with an appropriate spline type; see Sec. 4.2. For example, we can approximate $\gamma_{4,1}^{1-}$ with a periodic cubic spline, cut the spline into three pieces at v_1, v_4, v_5 , and reuse them in assembling other Jordan curves that share common boundaries with $\gamma_{4,1}^{1-}$.

Lastly, we combine topological and geometric data structures to form an approximation of Γ in Notation 4.26; see Fig. 3 and the last paragraph of Sec. 4.3 for a summary of our design of a discrete boundary representation of \mathcal{M} .

4.1. Representing the topology of Γ

At the center of representing the *unoriented* point set $\chi(\Gamma)$ and *oriented* boundary curves of the Yin sets is

Definition 4.2. A *graph* is a triple $G = (V, E, \psi)$ where V is a set of *vertices*, E a set of *edges*, and $\psi : E \rightarrow V \times V$ the *incidence function* given by $\psi(e) = (v_s, v_t)$, where the vertices v_s and v_t are called the *source* and *target* of the edge e , respectively. G is *undirected* if we do not distinguish the source and target for any edge; G is *directed* if we do for all edges. The *set of edges incident to* $v \in V$ is

$$E_v := \{e \in E : \psi(e) = (v, \cdot) \text{ or } (\cdot, v)\}. \quad (4.2)$$

An edge $e \in E$ is a *self-loop* if $\psi(e) = (v, v)$ for some vertex v . The *degree or valence of a vertex*, written $\#E_v$, is the number of edges incident to v , with each self-loop counted twice. A *subgraph* of $G = (V, E, \psi)$ is a graph $G' = (V', E', \psi')$ such that $V' \subseteq V$, $E' \subseteq E$, and $\psi' = \psi|_{E'}$.

Definition 4.3 (Types of subgraphs). A *walk* is a sequence of edges joining a sequence of vertices. A *trail* is a walk where all edges are distinct. A *circuit* is a non-empty trail where the first and last vertices coincide. A *cycle* is a circuit where only the first and last vertices coincide.

Definition 4.4. A *planar graph* is a graph $G = (V, E, \psi)$ satisfying

- (a) each vertex in V is a point in \mathbb{R}^2 ,
- (b) each edge in E is a curve $\gamma : [0, 1] \rightarrow \mathbb{R}^2$ whose endpoints are in V ,
- (c) two different edges/curves in E do not intersect except at vertices in V ,

12 *Y. Tan & Y. Qian & Z. Li & Q. Zhang*

(d) the incidence function is given by $\forall \gamma \in E$, $\psi(\gamma) := (\gamma(0), \gamma(1))$.

Any planar graph admits a dual graph, which promptly yields, for two given Yin sets, their adjacency [9, Sec. 4.6]. This feature is helpful in coupling IT methods with main flow solvers.

Definition 4.5. A *junction of the interface* $\chi(\Gamma)$ is a point $p \in \chi(\Gamma)$ such that, for any $\epsilon > 0$, the intersection of $\chi(\Gamma)$ with the ϵ -open ball centered at p is *not* homeomorphic to the interval $(0, 1)$. The set of all junctions of $\chi(\Gamma)$ is denoted by J_Γ .

In particular, T junctions and Y junctions are junctions of degree 3 described in the caption of Fig. 1; an X junction is a junction of degree 4. Since we approximate $\chi(\Gamma)$ with cubic splines, a curve is said to be *smooth* if it is \mathcal{C}^4 . If quintic splines were employed, it would be appropriate to define a smooth curve as \mathcal{C}^6 .

Definition 4.6. A *kink of the interface* $\chi(\Gamma)$ is a point $p \in (\chi(\Gamma) \setminus J_\Gamma)$ such that $\chi(\Gamma)$ is not smooth at p . The set of all kinks of $\chi(\Gamma)$ is denoted by K_Γ .

Recalling from Sec. 2 that a curve segment and its corresponding open curve are different, we represent the topology and geometry of the interface $\chi(\Gamma)$ by

Definition 4.7 (Interface graph). The *interface graph* of N_p pairwise disjoint Yin sets is an undirected planar graph $G_\Gamma = (V_\Gamma, E_\Gamma, \psi_\Gamma)$ constructed as follows.

- (a) Initialize $V_\Gamma \leftarrow J_\Gamma \cup K_\Gamma$ and $E_\Gamma \leftarrow \emptyset$;
- (b) Each curve γ in $\Gamma_E := \chi(\Gamma) \setminus (J_\Gamma \cup K_\Gamma)$ must be one of the three types:
 - (i) Jordan curves, (ii) open curves whose corresponding curve segments are not closed, and (iii) open curves whose corresponding curve segments are Jordan.
 - For γ of type (i), add $\gamma(\frac{1}{2})$ into V_Γ and add γ as a self-loop into E_Γ .
 - For γ of type (ii), add into E_Γ its corresponding curve segment;
 - For γ of type (iii), add γ as a self-loop into E_Γ if $\gamma(0) = \gamma(1)$ is a kink; otherwise add $\gamma(\frac{1}{2})$ into V_Γ and add into E_Γ the two curve segments $\gamma([0, \frac{1}{2}])$ and $\gamma([\frac{1}{2}, 1])$.
- (c) Deduce the incidence function ψ_Γ of G_Γ from (d) of Definition 4.4.

The point $v_\gamma := \gamma(\frac{1}{2})$ of types (i, iii) in (b) is the *basepoint of the Jordan curve* γ .

See Fig. 2 for an illustration of the construction steps in Definition 4.7. For γ of type (i) in (b), we add into V_Γ the basepoint v_γ of the Jordan curve so that $\psi_\Gamma(\gamma) = (v_\gamma, v_\gamma)$. For type (iii) where multiple Jordan curves intersect at a single junction, it is necessary to add the basepoint of each Jordan curve into V_Γ ; otherwise it would be difficult to enforce the smoothness of a trail that spans multiple Jordan curves, cf. the trail $(e_{15}, e_{10}, e_{11}, e_{16})$ in Fig. 2.

By Theorem 2.2, each boundary Jordan curve $\gamma_{i,j}^k$ of a Yin set induces a directed cycle $C_{i,j}^k$, of which the constituting edges come from the interface graph G_Γ and directions of these edges are determined by the orientation of $\gamma_{i,j}^k$.

Notation 4.8. Denote by $C_{i,j}^k$ the (i, j, k) th directed cycle of the oriented boundary Jordan curve $\gamma_{i,j}^k$. Analogous to Notation 4.1, the (directed) cycle sets of Γ are denoted by $C_{i,j} := \{C_{i,j}^k\}$, $C_i := \{C_{i,j} : j = 1, \dots, N_{\mathcal{M}_i}\}$, and $C := \{C_i : i = 1, \dots, N_p\}$.

See the third column of Fig. 2(c) for all directed cycles of the Yin sets in Fig. 2(a). In particular, the counter-clockwise self-loop with basepoint v_2 is not in Fig. 2(b) because the bounded Yin set it represents does not belong to \mathcal{M} , nor are the two counter-clockwise cycles adjacent at the junction v_7 .

4.2. Approximating the geometry of $\chi(\Gamma)$

The interface topology is captured in ψ_Γ and C while its geometry in E_Γ .

Definition 4.9. For the interface $\chi(\Gamma)$, the *spline edge set* S_E is a set of splines that approximate curves in E_Γ and the *set of marker sequences* is

$$E_X := \{(v_i, X_1, \dots, X_{N_\gamma-1}, v_j) : \gamma \in E_\Gamma, \psi_\Gamma(\gamma) = (v_i, v_j)\}, \quad (4.3)$$

where $X_1, \dots, X_{N_\gamma-1}$ are points on γ selected as its *interior markers*.

Besides the obvious isomorphisms $S_E \cong E_X \cong E_\Gamma$, any two corresponding elements in S_E and E_Γ are required to be homeomorphic, which can be satisfied by a sufficient number of interior markers for the sequence in E_X . The following subsections concern two types of splines that will be useful for generating S_E from S_{CT} in Definition 4.25.

4.2.1. Cubic splines

The *arc length* of a \mathcal{C}^1 curve $\gamma : [0, 1] \rightarrow \mathbb{R}^2$ is a continuous function $s_\gamma : [0, 1] \rightarrow [0, L_\gamma]$ where $s_\gamma(l) := \int_0^l \sqrt{x'_\gamma(\tau)^2 + y'_\gamma(\tau)^2} d\tau$ and L_γ is the total length of γ . Reparametrize γ as $[0, L_\gamma] \rightarrow \mathbb{R}^2$, consider γ as two coordinate functions $x_\gamma, y_\gamma : [0, L_\gamma] \rightarrow \mathbb{R}$ with the same domain, and we can approximate x_γ and y_γ separately via

Definition 4.10 (Space of spline functions). For a strictly increasing sequence $X_b := (x_i)_{i=0}^N$ that partitions $[a, b]$ as

$$a = x_0 < x_1 < \dots < x_N = b, \quad (4.4)$$

the space of *spline functions of degree $m \in \mathbb{N}$ and smoothness class $j \in \mathbb{N}$* over X_b is

$$\mathbb{S}_m^j(X_b) := \{s \in \mathcal{C}^j[a, b] : \forall i = 0, \dots, N-1, s|_{[x_i, x_{i+1}]} \in \mathbb{P}_m\}, \quad (4.5)$$

where \mathbb{P}_m is the space of polynomials with degree no more than m and each x_i is called a *breakpoint* of s .

\mathbb{S}_3^2 is probably the most popular class of spline functions. By (4.5), the restriction of any $s \in \mathbb{S}_3^2$ on a subinterval is a cubic polynomial and thus $4N$ coefficients need to be determined. In interpolating a function $f : [a, b] \rightarrow \mathbb{R}$ by $s \in \mathbb{S}_3^2$, the number of equations given by the interpolation conditions at all breakpoints and by the continuity requirements at interior breakpoints is respectively $N + 1$ and $3(N - 1)$, leading to a total of $4N - 2$ equations. The last two equations come from

Definition 4.11 (Types of cubic spline functions). A *periodic cubic spline function* is a spline function $s \in \mathbb{S}_3^2$ satisfying $s(0) = s(1)$, $s'(0) = s'(1)$, and $s''(0) = s''(1)$. A *not-a-knot cubic spline function* is a spline function $s \in \mathbb{S}_3^2$ such that $s'''(x)$ exists at $x = x_1$ and $x = x_{N-1}$, cf. Definition 4.10.

A *spline* (curve) is a pair of spline functions as its coordinate functions. Each smooth closed curve in Γ_E is not necessarily Jordan due to potential self-intersections, but can be nonetheless approximated by a periodic cubic spline. Similarly, each smooth curve segment in Γ_E is approximated by a not-a-knot cubic spline. In both cases, the *cumulative chordal length* is a discrete counterpart of the arc length of $\gamma \in \Gamma_E$ from a sequence of distinct markers $(\mathbf{X}_i)_{i=0}^N$ on γ :

$$l_0 = 0; \quad \forall i = 1, \dots, N, \quad l_i = l_{i-1} + \|\mathbf{X}_i - \mathbf{X}_{i-1}\|_2, \quad (4.6)$$

where $\|\cdot\|_2$ denotes the Euclidean 2-norm. Both having $(l_i)_{i=0}^N$ as the breakpoints, the two coordinate spline functions are determined *separately* and then combined as the interpolatory spline of γ .

4.2.2. Periodic cubic splines with (r, h) -regularity

The representation error of a smooth closed curve by two periodic cubic splines is given by

Theorem 4.12. A periodic spline $p \in \mathbb{S}_3^2(X_b)$ that interpolates a periodic function $f \in \mathcal{C}^2([a, b]) \cap \mathcal{C}^4([a, b] \setminus X_b)$ at X_b can be uniquely determined and satisfies

$$\forall x \in [a, b], \quad \forall j = 0, 1, 2, \quad \left| p^{(j)}(x) - f^{(j)}(x) \right| \leq c_j h^{4-j} \max_{\xi \in [a, b] \setminus X_b} \left| f^{(4)}(\xi) \right|, \quad (4.7)$$

where the constants are given by $c_0 = \frac{1}{16}$, $c_1 = c_2 = \frac{1}{2}$, and $h := \max_{i=1}^N |x_i - x_{i-1}|$.

Proof. See [13, Section 2.2.1]. \square

The spline-fitting process is further guaranteed to be well conditioned if, for some $r > 0$ not too small, the breakpoint sequence satisfies

Definition 4.13 (The (r, h) -regularity). A breakpoint sequence is said to be (r, h) -regular if the distance between each pair of adjacent breakpoints is within the range $[rh, h]$ where $h > 0$ and $r \in (0, 1]$.

The (r, h) -regularity in Definition 4.13 is all periodic splines need for spline-fitting.

Definition 4.14 (The (r, h) -regularity for periodic splines). A breakpoint sequence X_b is (r, h) -regular for periodic splines if X_b is (r, h) -regular.

However, as for not-a-knot splines, the (r, h) -regularity in Definition 4.13 is not sufficient for the well-conditioning of the spline-fitting process. We will further explain that in the next subsection.

4.2.3. Not-a-knot cubic splines with (r, h) -regularity

It turns out that not-a-knot cubic splines are fundamentally different from periodic cubic splines with respect to algorithms and analysis in the context of multiphase IT. These differences are caused by the topological distinction of these two cases: smooth closed curves approximated by periodic splines are *cycles* while smooth curve segments approximated by not-a-knot splines are *not*.

Lemma 4.15. Let $p \in \mathbb{S}_3^2(X_b)$ be a not-a-knot spline interpolating a function f at the nodes X_b . Then the second derivatives $M_i = p''(x_i)$ satisfy:

$$\forall i = 1, \dots, N-1, \quad \mu_i M_{i-1} + 2M_i + \lambda_i M_{i+1} = 6f[x_{i-1}, x_i, x_{i+1}], \quad (4.8)$$

$$\lambda_1 M_0 - M_1 + \mu_1 M_2 = 0, \quad \lambda_{N-1} M_{N-2} - M_{N-1} + \mu_{N-1} M_N = 0, \quad (4.9)$$

where

$$\forall i = 1, \dots, N-1, \quad \mu_i = \frac{x_i - x_{i-1}}{x_{i+1} - x_{i-1}}, \quad \lambda_i = \frac{x_{i+1} - x_i}{x_{i+1} - x_{i-1}}, \quad (4.10)$$

and the divided difference is recursively given by

$$f[x] := f(x); \quad f[x_0, x_1, \dots, x_j] := \frac{f[x_1, \dots, x_j] - f[x_0, \dots, x_{j-1}]}{x_j - x_0}. \quad (4.11)$$

Proof. Taylor expansion of $p(x)$ at x_i yields

$$p(x) = f_i + p'(x_i)(x - x_i) + \frac{M_i}{2}(x - x_i)^2 + \frac{p'''(x_i)}{6}(x - x_i)^3. \quad (4.12)$$

Differentiate (4.12) twice at $x \in (x_i, x_{i+1}]$, set $x = x_{i+1}$, and we have $p'''(x_i) = \frac{M_{i+1} - M_i}{x_{i+1} - x_i}$, the substitution of which into (4.12) yields

$$p'(x_i) = f[x_i, x_{i+1}] - \frac{1}{6}(M_{i+1} + 2M_i)(x_{i+1} - x_i). \quad (4.13)$$

Similarly, for $x \in [x_{i-1}, x_i)$, differentiate (4.12) twice, set $x = x_{i-1}$, and we have $p'''(x_i) = \frac{M_{i-1} - M_i}{x_{i-1} - x_i}$ and

$$p'(x_i) = f[x_{i-1}, x_i] - \frac{1}{6}(M_{i-1} + 2M_i)(x_{i-1} - x_i). \quad (4.14)$$

Then (4.8) follows from subtracting (4.13) from (4.14) and applying (4.11).

16 *Y. Tan & Y. Qian & Z. Li & Q. Zhang*

By Definition 4.11, the not-a-knot boundary condition requires continuity of $p'''(x)$ at both x_1 and x_{N-1} , i.e.,

$$\forall i \in \{1, N-1\}, \quad \frac{M_{i+1} - M_i}{x_{i+1} - x_i} = \frac{M_{i-1} - M_i}{x_{i-1} - x_i},$$

which, when multiplied by $\frac{(x_{i+1}-x_i)(x_i-x_{i-1})}{x_{i+1}-x_{i-1}}$, yields (4.9). \square

Lemma 4.16. *A not-a-knot spline $p \in \mathbb{S}_3^2(X_b)$ interpolating $f \in \mathcal{C}^2([a, b])$ satisfies*

$$\forall x \in [a, b], \quad |p''(x)| \leq \left(\frac{6}{r_b} + 3 \right) \max_{\xi \in [a, b]} |f''(\xi)|, \quad (4.15)$$

where r_b only depends on X_b and is given by

$$r_b(X_b) := \min \left(\frac{x_2 - x_1}{x_1 - x_0}, \frac{x_{N-1} - x_{N-2}}{x_N - x_{N-1}} \right). \quad (4.16)$$

Proof. Since p'' is piecewise linear on $[x_i, x_{i+1}]$, its maximum absolute value must occur at some breakpoint x_j .

In the case of $j = 2, \dots, N-2$, Lemma 4.15 yields

$$\begin{aligned} 2M_j &= 6f[x_{j-1}, x_j, x_{j+1}] - \mu_j M_{j-1} - \lambda_j M_{j+1} \\ \implies 2|M_j| &\leq 6|f[x_{j-1}, x_j, x_{j+1}]| + (\mu_j + \lambda_j)|M_j| \\ \implies \exists \xi \in (x_{j-1}, x_{j+1}) \text{ s.t. } |M_j| &\leq 3|f''(\xi)| \\ \implies |M_j| &\leq 3 \max_{\xi \in [a, b]} |f''(\xi)|, \end{aligned}$$

where the third line follows from the partition of unity $\mu_j + \lambda_j = 1$ and the mean value property of divided differences.

In the cases of $j = 1, 0$, we have, from (4.9) and (4.8),

$$\begin{aligned} (2 + \frac{x_1-x_0}{x_2-x_1})M_1 &= 6f[x_0, x_1, x_2] + \frac{(x_1-x_0)-(x_2-x_1)}{x_2-x_1}M_2 \\ \implies |2 + \frac{x_1-x_0}{x_2-x_1}||M_1| &\leq 6|f[x_0, x_1, x_2]| + (\frac{x_1-x_0}{x_2-x_1} + 1)|M_2| \\ \implies |M_1| &\leq 6|f[x_0, x_1, x_2]| \leq 3 \max_{\xi \in [a, b]} |f''(\xi)|; \\ M_0 &= \frac{x_1-x_0}{x_2-x_1}(M_1 - M_2) + M_1 \\ \implies |M_0| &\leq \frac{1}{r_b}(|M_1| + |M_2|) + |M_1| \leq \left(\frac{2}{r_b} + 1 \right) \max_{j \notin \{0, N\}} |M_j| \\ \implies |M_0| &\leq \left(\frac{6}{r_b} + 3 \right) \max_{\xi \in [a, b]} |f''(\xi)|. \end{aligned}$$

The conclusion for $j = N-1, N$ follows from similar arguments. \square

As r_b decrease, the upper bound of $|p''(x)|$ increases. Hence it is natural to demand a lower bound on r_b so that $|p''(x)|$ is not too large.

Definition 4.17 (The (r, h) -regularity for not-a-knot splines). A breakpoint sequence X_b is (r, h) -regular for not-a-knot splines if X_b is (r, h) -regular and there exists $r_b^* > 1$ such that $r_b^* \leq r_b(X_b)$, where r_b is given by (4.16).

Lemma 4.18 and Theorem 4.19 illustrate that the (r, h) -regularity for not-a-knot splines indeed guarantees the well-conditioning.

Lemma 4.18. *There exists a unique not-a-knot spline $p \in \mathbb{S}_3^2(X_b)$ that interpolates any $f \in \mathcal{C}^2([a, b])$ over any (r, h) -regular sequence X_b for not-a-knot splines as in Definition 4.17.*

Proof. Lemma 4.15 leads to

$$A\mathbf{M} := \begin{bmatrix} \lambda_1 & -1 & \mu_1 & & & \\ \mu_1 & 2 & \lambda_1 & & & \\ & \mu_2 & 2 & \lambda_2 & & \\ & & & \ddots & & \\ & & & & \mu_{N-2} & 2 & \lambda_{N-2} \\ & & & & & \mu_{N-1} & 2 & \lambda_{N-1} \\ & & & & & & \lambda_{N-1} & -1 & \mu_{N-1} \end{bmatrix} \begin{bmatrix} M_0 \\ M_1 \\ M_2 \\ \vdots \\ M_{N-2} \\ M_{N-1} \\ M_N \end{bmatrix} = \mathbf{b}, \quad (4.17)$$

where μ_i, λ_i are defined in (4.10), and

$$\begin{aligned} \forall i = 1, \dots, N-1, \quad b_i &= 6f[x_{i-1}, x_i, x_{i+1}], \\ b_0 &= 0, \quad b_N = 0. \end{aligned}$$

The (r, h) -regularity of sequence X_b yields

$$\frac{r}{1+r} \leq \mu_i \leq \frac{1}{1+r}, \quad \frac{r}{1+r} \leq \lambda_i \leq \frac{1}{1+r}, \quad (4.18)$$

and $r_b(X_b) \geq r_b^* > 1$ implies

$$\lambda_1 > \mu_1, \quad \mu_{N-1} > \lambda_{N-1}, \quad (4.19)$$

which, together with (4.18), shows that the matrix A in (4.17) is strictly diagonally dominant by columns and thus non-singular. Therefore, the linear system admits a unique solution of the set of second derivatives $\{M_i\}_{i=0}^N$, which uniquely determines the not-a-knot spline function $p \in \mathbb{S}_3^2$. \square

Theorem 4.19. *Over an (r, h) -regular sequence X_b of breakpoints for not-a-knot splines, the not-a-knot spline $p \in \mathbb{S}_3^2(X_b)$ that interpolates any $f \in \mathcal{C}^2([a, b]) \cap \mathcal{C}^4([a, b] \setminus X_b)$ satisfies*

$$\forall x \in [a, b], \quad \forall j = 0, 1, 2, \quad \left| p^{(j)}(x) - f^{(j)}(x) \right| \leq c_j h^{4-j} \max_{\xi \in [a, b] \setminus X_b} \left| f^{(4)}(\xi) \right|, \quad (4.20)$$

where the constants are given by $c_0 = \frac{3}{32r_b} + \frac{1}{16}$, $c_1 = c_2 = \frac{3}{4r_b} + \frac{1}{2}$.

Proof. It follows Lemma 4.18 that the spline p exists and is unique.

For $j = 2$, we interpolate $f''(x)$ with some $\tilde{p} \in \mathbb{S}_1^0$ and integrate \tilde{p} twice to get $\hat{p} \in \mathbb{S}_3^2$ so that \hat{p}'' interpolates f'' over (4.4). The Cauchy remainder theorem of polynomial interpolation gives

$$\begin{aligned} \exists \xi_i \in (x_i, x_{i+1}), \quad \text{s.t. } \forall x \in [x_i, x_{i+1}], \\ |f''(x) - \tilde{p}(x)| \leq \frac{1}{2} |f^{(4)}(\xi_i)| |(x - x_i)(x - x_{i+1})| \end{aligned}$$

18 *Y. Tan & Y. Qian & Z. Li & Q. Zhang*

and hence we have

$$|f''(x) - \hat{p}''(x)| \leq \frac{h^2}{8} \max_{x \in [a, b] \setminus X_b} |f^{(4)}(x)|. \quad (4.21)$$

Since $\hat{p}(x) \in \mathbb{S}_3^2$, $p(x) - \hat{p}(x)$ must interpolate $f(x) - \hat{p}(x)$. Then Lemma 4.16 yields

$$\forall x \in [a, b], \quad |p''(x) - \hat{p}''(x)| \leq \left(\frac{6}{r_b} + 3 \right) \max_{\xi \in [a, b]} |f''(\xi) - \hat{p}''(\xi)|,$$

which, together with the triangular inequality, gives

$$\begin{aligned} \forall x \in [a, b], \quad |f''(x) - p''(x)| &\leq \left(\frac{6}{r_b} + 4 \right) \max_{\xi \in [a, b]} |f''(\xi) - \hat{p}''(\xi)| \\ &\leq \left(\frac{3}{4r_b} + \frac{1}{2} \right) h^2 \max_{\xi \in [a, b] \setminus X_b} |f^{(4)}(\xi)|, \end{aligned} \quad (4.22)$$

where the second step follows from (4.21).

For $j = 1$, the interpolation conditions give $f(x) - p(x) = 0$ for $x = x_i, x_{i+1}$ and Rolle's theorem implies $f'(\xi_i) - p'(\xi_i) = 0$ for some $\xi_i \in (x_i, x_{i+1})$. Then the second fundamental theorem of calculus yields

$$\forall x \in [x_i, x_{i+1}], \quad f'(x) - p'(x) = \int_{\xi_i}^x (f''(t) - p''(t)) dt,$$

which, together with the integral mean value theorem and (4.22), gives

$$\begin{aligned} \forall x \in [a, b], \quad |f'(x) - p'(x)|_{x \in [x_i, x_{i+1}]} &= |x - \xi_i| |f''(\eta_i) - p''(\eta_i)| \\ &\leq \left(\frac{3}{4r_b} + \frac{1}{2} \right) h^3 \max_{\xi \in [a, b] \setminus X_b} |f^{(4)}(\xi)|. \end{aligned}$$

For $j = 0$, the interpolation of $f(x) - p(x)$ with some $\bar{p} \in \mathbb{S}_1^0$ dictates $\bar{p}(x) \equiv 0$ for any $x \in [a, b]$. Hence

$$\begin{aligned} \forall x \in [x_i, x_{i+1}], \quad |f(x) - p(x)| &= |f(x) - p(x) - \bar{p}| \\ &\leq \frac{1}{8} (x_{i+1} - x_i)^2 \max_{\xi \in (x_i, x_{i+1})} |f''(\xi) - p''(\xi)| \\ &\leq \left(\frac{3}{32r_b} + \frac{1}{16} \right) h^4 \max_{\xi \in [a, b] \setminus X_b} |f^{(4)}(\xi)|, \end{aligned}$$

where the first inequality follows from the Cauchy remainder theorem and the second inequality from (4.22). \square

By Theorems 4.12 and 4.19, the representation error of a not-a-knot spline depends on the value of r_b while that of a periodic spline does not. At the core of this difference is the topological fact that a periodic spline is homeomorphic to a cycle while a not-a-knot spline to an interval.

4.2.4. Perturbing breakpoints of periodic and not-a-knot cubic splines

For the spline $S : \mathcal{L} \rightarrow \mathbb{R}^2$, denote by $\mathcal{L} := [l_0, l_N]$ the interval of the cumulative chordal length and l_0, l_1, \dots, l_N the knots such that $\Delta l_i := l_{i+1} - l_i = O(h)$ and $S(l_{i+1}) - S(l_i) = \mathbf{O}(h)$. An $O(\epsilon)$ perturbation with $\epsilon \ll h$ to knots of $S(l)$ yields a new spline $\hat{S}(\hat{l})$ with $\hat{l} \in \hat{\mathcal{L}} := [\hat{l}_0, \hat{l}_N]$ and knots $\hat{l}_0, \hat{l}_1, \dots, \hat{l}_N$ satisfying $\Delta \hat{l}_i := \hat{l}_{i+1} - \hat{l}_i = O(h)$,

$$\hat{S}(\hat{l}_i) - S(l_i) = \mathbf{O}(\epsilon), \text{ and } \Delta \hat{l}_i - \Delta l_i = O(\epsilon). \quad (4.23)$$

Construct a bijection $v : \mathcal{L} \rightarrow \hat{\mathcal{L}}$ that maps each $[l_i, l_{i+1}]$ to $[\hat{l}_i, \hat{l}_{i+1}]$, i.e.,

$$\hat{l}|_{[\hat{l}_i, \hat{l}_{i+1}]} = v|_{[l_i, l_{i+1}]}(l) = \frac{\Delta \hat{l}_i}{\Delta l_i} (l - l_i) + \hat{l}_i. \quad (4.24)$$

Then, the numerical stability of fitting a periodic spline or a not-a-knot spline is guaranteed by Lemma 4.20 and 4.21.

Lemma 4.20. *Let $\{\mathbf{X}_i\}_{i=0}^N$ be an (r, h) -regular sequence for periodic or not-a-knot splines. Perform an $O(\epsilon)$ perturbation to a single breakpoint \mathbf{X}_j ($j = 1, \dots, N-1$), and denote by $S : \mathcal{L} \rightarrow \mathbb{R}^2$ and $\hat{S} : \hat{\mathcal{L}} \rightarrow \mathbb{R}^2$ the cubic splines before and after the perturbation, respectively. Then, we have*

$$\int_{l_0}^{l_{j-1}} \|S(l) - \hat{S}(v(l))\|_2 dl + \int_{l_{j+1}}^{l_N} \|S(l) - \hat{S}(v(l))\|_2 dl = O(\epsilon h),$$

where the bijection v maps each $[l_i, l_{i+1}]$ to $[\hat{l}_i, \hat{l}_{i+1}]$ as defined in (4.24).

Proof. The key lies in the strictly diagonal dominance property of the linear system. We only prove the conclusion for not-a-knot cubic splines and the case of periodic splines can be proven similarly.

The cumulative chordal length (4.6) and the (r, h) -regularity yield

$$\begin{aligned} \forall i \notin \{j-1, j\}, \quad \Delta \hat{l}_i - \Delta l_i &= (\hat{l}_{i+1} - \hat{l}_i) - (l_{i+1} - l_i) = 0, \\ \Delta \hat{l}_{j-1} - \Delta l_{j-1} &= (\hat{l}_j - \hat{l}_{j-1}) - (l_j - l_{j-1}) = O(\epsilon), \\ \Delta \hat{l}_j - \Delta l_j &= (\hat{l}_{j+1} - \hat{l}_j) - (l_{j+1} - l_j) = O(\epsilon), \end{aligned} \quad (4.25)$$

and the bijection v can be simplified as

$$\begin{aligned} \forall i = 0, \dots, j-2, \quad v|_{[l_i, l_{i+1}]}(l) &= l, \\ \forall i = j+1, \dots, N-1, \quad v|_{[l_i, l_{i+1}]}(l) &= l - l_i + \hat{l}_i = l - l_{j+1} + \hat{l}_{j+1}. \end{aligned} \quad (4.26)$$

Lemma 4.15 and 4.18 give a linear system on the second derivatives $M_i := S''(l_i)$ by

$$A\mathbf{M} = \mathbf{b},$$

where A is defined in (4.17), and

$$\begin{aligned} \forall i = 1, \dots, N-1, \quad b_i &= 6S[l_{i-1}, l_i, l_{i+1}], \\ b_0 &= \mathbf{0}, \quad b_N = \mathbf{0}. \end{aligned} \quad (4.27)$$

For each $i = 0, \dots, N-1$, the form of S on $[l_i, l_{i+1}]$ is

$$\begin{aligned} S|_{[l_i, l_{i+1}]}(l) &= \frac{(l_{i+1}-l)^3}{6\Delta l_i} M_i + \frac{(l-l_i)^3}{6\Delta l_i} M_{i+1} + \left(\frac{l_{i+1}-l}{\Delta l_i}\right) S(l_i) + \left(\frac{l-l_i}{\Delta l_i}\right) S(l_{i+1}) \\ &\quad - \frac{(\Delta l_i)^2}{6} \left[\left(\frac{l_{i+1}-l}{\Delta l_i}\right) M_i + \left(\frac{l-l_i}{\Delta l_i}\right) M_{i+1} \right]. \end{aligned} \quad (4.28)$$

We construct \hat{S} by repeated arguments. Denote by $\hat{M}_i := \hat{S}''(\hat{l}_i)$ the second derivative of \hat{S} and we have the linear system

$$\hat{A}\hat{\mathbf{M}} = \hat{\mathbf{b}},$$

20 *Y. Tan & Y. Qian & Z. Li & Q. Zhang*

where the elements $\hat{\mu}_i$, $\hat{\lambda}_i$, and \hat{b}_i are analogous to those in (4.10) and (4.27). It follows from (4.25) that $\hat{\mu}_i, \hat{\lambda}_i$ satisfy

$$\begin{aligned} \forall i \notin \{j-1, j, j+1\}, \quad \hat{\mu}_i &= \mu_i, \quad \hat{\lambda}_i = \lambda_i, \\ \forall i \in \{j-1, j, j+1\}, \quad \hat{\mu}_i - \mu_i &= O\left(\frac{\epsilon}{h}\right), \quad \hat{\lambda}_i - \lambda_i = O\left(\frac{\epsilon}{h}\right), \end{aligned} \quad (4.29)$$

since

$$\begin{aligned} \hat{\mu}_{j+1} - \mu_{j+1} &= \frac{\hat{l}_{j+1} - \hat{l}_j}{\hat{l}_{j+2} - \hat{l}_j} - \frac{l_{j+1} - l_j}{l_{j+2} - l_j} \\ &= \frac{l_{j+1} - l_j + O(\epsilon)}{l_{j+2} - l_j + O(\epsilon)} - \frac{l_{j+1} - l_j}{l_{j+2} - l_j} = O\left(\frac{\epsilon}{h}\right), \end{aligned}$$

and the other terms in (4.29) can be similarly obtained. Also, (4.27) gives

$$\forall i \notin \{j-1, j, j+1\}, \quad \hat{b}_i = b_i, \quad \forall i \in \{j-1, j, j+1\}, \quad \hat{b}_i - b_i = \mathbf{O}\left(\frac{\epsilon}{h^2}\right). \quad (4.30)$$

Hence, for each $i = 0, \dots, N-1$, the form of \hat{S} on $[\hat{l}_i, \hat{l}_{i+1}]$ is

$$\begin{aligned} \hat{S}|_{[\hat{l}_i, \hat{l}_{i+1}]}(\hat{l}) &= \frac{(\hat{l}_{i+1} - \hat{l})^3}{6\Delta\hat{l}_i} \hat{M}_i + \frac{(\hat{l} - \hat{l}_i)^3}{6\Delta\hat{l}_i} \hat{M}_{i+1} + \left(\frac{\hat{l}_{i+1} - \hat{l}}{\Delta\hat{l}_i}\right) \hat{S}(\hat{l}_i) + \left(\frac{\hat{l} - \hat{l}_i}{\Delta\hat{l}_i}\right) \hat{S}(\hat{l}_{i+1}) \\ &\quad - \frac{(\Delta\hat{l}_i)^2}{6} \left[\left(\frac{\hat{l}_{i+1} - \hat{l}}{\Delta\hat{l}_i}\right) \hat{M}_i + \left(\frac{\hat{l} - \hat{l}_i}{\Delta\hat{l}_i}\right) \hat{M}_{i+1} \right]. \end{aligned} \quad (4.31)$$

Next we show $\|A^{-1}\|_1 = O(1)$, where $\|\cdot\|_1$ denotes the matrix 1-norm. Decompose A into its diagonal and off-diagonal parts by

$$A = D - E,$$

where $D = \text{diag}(\lambda_1, 2, \dots, 2, \mu_{N-1})$ is the diagonal matrix, E has entries $E_{ij} = -a_{ij}$ for $i \neq j$ and $E_{ii} = 0$. Then

$$A^{-1} = (D - E)^{-1} = D^{-1}(I - ED^{-1})^{-1} = D^{-1} \sum_{k=0}^{\infty} (ED^{-1})^k,$$

where the last equality comes from the Neumann series and the fact that

$$\|ED^{-1}\|_1 = \max_{1 \leq j \leq N} \sum_{\substack{i=1 \\ i \neq j}}^n \frac{|a_{ij}|}{|a_{jj}|} \leq \max\left(\frac{1 + \frac{1}{1+r}}{2}, \frac{1}{r_b^*}\right) < 1,$$

where the second step follows from (4.17), (4.18), and $r_b \geq r_b^*$ in Definition 4.17. Therefore, we have

$$\|A^{-1}\|_1 \leq \|D^{-1}\|_1 \sum_{k=0}^{\infty} \|ED^{-1}\|_1^k \leq \frac{\|D^{-1}\|_1}{1 - \|ED^{-1}\|_1} = \frac{\max\left(\frac{1}{\lambda_1}, \frac{1}{\mu_{N-1}}\right)}{1 - \|ED^{-1}\|_1} = O(1), \quad (4.32)$$

where the last step comes from (4.18). Subtract linear systems before and after the perturbation and we have

$$\begin{aligned} \mathbf{b} - \hat{\mathbf{b}} &= \mathbf{A}\mathbf{M} - \hat{\mathbf{A}}\hat{\mathbf{M}} = \mathbf{A}\mathbf{M} - \mathbf{A}\hat{\mathbf{M}} + \mathbf{A}\hat{\mathbf{M}} - \hat{\mathbf{A}}\hat{\mathbf{M}} \\ \implies \mathbf{A}(\mathbf{M} - \hat{\mathbf{M}}) &= \mathbf{b} - \hat{\mathbf{b}} - (\mathbf{A} - \hat{\mathbf{A}})\hat{\mathbf{M}}, \end{aligned}$$

which implies

$$\|\mathbf{M} - \hat{\mathbf{M}}\|_1 \leq \|A^{-1}\|_1 \left(\|\mathbf{b} - \hat{\mathbf{b}}\|_1 + \|A - \hat{A}\|_1 \|\hat{\mathbf{M}}\|_1 \right) = O\left(\frac{\epsilon}{h^2}\right), \quad (4.33)$$

where the last equation follows from (4.29), (4.30), (4.32), and Lemma 4.16.

We complete the proof by

$$\begin{aligned} & \int_{l_0}^{l_{j-1}} \|S(l) - \hat{S}(v(l))\|_2 \, dl + \int_{l_{j+1}}^{l_N} \|S(l) - \hat{S}(v(l))\|_2 \, dl \\ &= \int_{l_0}^{l_{j-1}} \|S(l) - \hat{S}(l)\|_2 \, dl + \int_{l_{j+1}}^{l_N} \|S(l) - \hat{S}(l - l_{j+1} + \hat{l}_{j+1})\|_2 \, dl \\ &= (\sum_{i=0}^{j-2} + \sum_{i=j+1}^{N-1}) \int_{l_i}^{l_{i+1}} \left\| \frac{(l_{i+1}-l)^3}{6\Delta l_i} (M_i - \hat{M}_i) + \frac{(l-l_i)^3}{6\Delta l_i} (M_{i+1} - \hat{M}_{i+1}) \right. \\ & \quad \left. - \frac{(\Delta l_i)^2}{6} \left[\left(\frac{l_{i+1}-l}{\Delta l_i} \right) (M_i - \hat{M}_i) + \left(\frac{l-l_i}{\Delta l_i} \right) (M_{i+1} - \hat{M}_{i+1}) \right] \right\|_2 \, dl \\ &\leq \sum_{i=0}^{N-1} \left(\frac{(\Delta l_i)^3}{8} \|M_i - \hat{M}_i\|_2 + \frac{(\Delta l_i)^3}{8} \|M_{i+1} - \hat{M}_{i+1}\|_2 \right) \\ &= O(h^3) \cdot \sum_{i=0}^N \|M_i - \hat{M}_i\|_2 \\ &\leq O(h^3) \cdot 2 \|\mathbf{M} - \hat{\mathbf{M}}\|_1 \\ &= O(\epsilon h), \end{aligned}$$

where the first step follows from (4.26), the second from (4.28) and (4.31), and the last from (4.33). \square

Lemma 4.20 demonstrates that a single-breakpoint perturbation will result in the area of the closed region bounded by the two spline curves being $O(\epsilon h)$. This fact will be applied in the error analysis of removing markers.

Lemma 4.21. *Let $\{\mathbf{X}_i\}_{i=0}^N$ be an (r, h) -regular sequence for periodic or not-a-knot splines. An $O(\epsilon)$ perturbation to each breakpoint causes an $O(\epsilon)$ error at each point of the fitted spline.*

Proof. By similar arguments as the proof of Lemma 4.20, it suffices to show $\|A^{-1}\|_\infty = O(1)$, where $\|\cdot\|_\infty$ denotes the matrix infinite norm.

For a periodic spline, the (r, h) -regularity of the breakpoint sequence indicates that the linear system is strictly diagonally dominant by rows, which further implies the conclusion. However, the matrix A in (4.17) for not-a-knot splines is not strictly diagonally dominant by rows. We construct a matrix C by

$$C = PA, \quad P := \begin{bmatrix} 1 & \frac{1}{2} & & & \\ 0 & 1 & & & \\ & & \ddots & & \\ & & & 1 & 0 \\ & & & \frac{1}{2} & 1 \end{bmatrix}. \quad (4.34)$$

22 *Y. Tan & Y. Qian & Z. Li & Q. Zhang*

Then, for the first row of C , we have

$$|c_{1,1}| = \lambda_1 + \frac{1}{2}\mu_1 > \mu_1 + \frac{1}{2}\lambda_1 = \sum_{j=2}^n |c_{1,j}|,$$

where the second inequality follows from $\lambda_1 > \mu_1$ in (4.19). Similarly, we can verify the condition for the last row, which implies that C is strictly diagonally dominant by rows and $\|C^{-1}\|_\infty = O(1)$. Hence, $\|A^{-1}\|_\infty \leq \|C^{-1}\|_\infty \|P\|_\infty = O(1)$. \square

4.3. Combining topology and geometry

While we definitely approximate a smooth closed curve by a periodic cubic spline, it might not be correct to approximate a curve segment $\gamma \in E_\Gamma$ by a not-a-knot spline fitted through markers on γ . In Fig. 2, the smoothness of $\gamma_{4,1}^{1-}$ is lost if the edges e_2, e_7, e_4 are approximated separately by not-a-knot splines. Our solution to this problem starts with

Definition 4.22. An *edge pairing of an undirected graph* $G = (V, E, \psi)$ is a set $R^{\text{EP}} := \{R_v^{\text{EP}} : v \in V\}$, where $R_v^{\text{EP}} \subseteq E_v \times E_v$, cf. (4.2), is a *set of pairs of adjacent edges at v* such that each self-loop $e \in E_v$ appears and only appears in the pair (e, e) while any other edge in E_v appears at most once across all pairs in R_v^{EP} .

Definition 4.23. The *smoothness indicator of an interface graph* G_Γ is an edge pairing of G_Γ such that, for each $v \in V_\Gamma$, each $(e_l, e_r) \in R_v^{\text{EP}}$ indicates that e_l and e_r connect smoothly at v ; in particular, $e_l = e_r$ corresponds to a smooth self-loop.

For the interface graph in Fig. 2(a), the smoothness indicator is given by

$$\begin{aligned} R_{v_1}^{\text{EP}} &= \{(e_2, e_4)\}, R_{v_3}^{\text{EP}} = \{(e_3, e_6)\}, R_{v_4}^{\text{EP}} = \{(e_2, e_7)\}, R_{v_5}^{\text{EP}} = \{(e_4, e_7)\}; \\ R_{v_6}^{\text{EP}} &= \{(e_1, e_9), (e_{12}, e_{14})\}, R_{v_7}^{\text{EP}} = \{(e_{10}, e_{11})\}, R_{v_8}^{\text{EP}} = \{(e_1, e_9), (e_{12}, e_{13})\}; \\ R_{v_2}^{\text{EP}} &= \{(e_8, e_8)\}, R_{v_{10}}^{\text{EP}} = \{(e_{10}, e_{15})\}, R_{v_{11}}^{\text{EP}} = \{(e_{11}, e_{16})\}; R_{v_9}^{\text{EP}} = \emptyset; \end{aligned} \quad (4.35)$$

where the first two lines correspond to T and X junctions, respectively. If there exist multiple edges that connect smoothly to a given e_l , we try to select an edge e_r such that e_r and e_l belong to the same cycle $C_{i,j}^k$.

Algorithm 1 decomposes the edge set of an undirected graph G into a set C_S of circuits and a set T_S of trails according to a given edge pairing R^{EP} .

Lemma 4.24. *Algorithm 1 stops and its post-conditions hold.*

Proof. By Sard's theorem and Definition 2.1, the total number of junctions and kinks is finite and thus E is also finite. Inside the three while loops, any edge added to the trail is immediately deleted and thus $\#E$ decreases strictly monotonically for each while loop. Therefore, eventually we have $E = \emptyset$ and the algorithm stops.

The trail \mathbf{e} is initialized at line 3 with a single edge. Then we grow \mathbf{e} by appending edges in R^{EP} to its left and right ends until there are no edges in E to be paired with these ends. During this process, removing e_r and e_l at lines 8 and 12

Algorithm 1 : $(C_S, T_S) = \text{decomposeEdgeSet}(G, R^{\text{EP}})$ **Input:** An undirected graph $G = (V, E, \psi)$ in Definition 4.2.and its edge pairing R^{EP} in Definition 4.22.**Output:** A set C_S of circuits and a set T_S of trails as in Definition 4.3.**Post-conditions:** (a) The edges in C_S and T_S partition E ;(b) $\forall \mathbf{e} \in (C_S \cup T_S), \forall (e_l, e_r) \text{ adjacent in } \mathbf{e}, \exists u \in V \text{ s.t. } (e_l, e_r) \in R_u^{\text{EP}}$.

```

1: Initialize  $C_S \leftarrow \emptyset; T_S \leftarrow \emptyset$ 
2: while  $E \neq \emptyset$  do
3:   Initialize a trail  $\mathbf{e} \leftarrow (e)$  with an arbitrary edge  $e \in E$ 
4:   Initialize  $(u_l, u_r) \leftarrow \psi(e)$  and remove  $e$  from  $E$ 
5:   Initialize  $e_1 \leftarrow e; e_m \leftarrow e; u_0 \leftarrow u_l; u_m \leftarrow u_r$  //  $\mathbf{e}$  contains  $m$  edges
6:   while  $\exists (e_m, e_r) \in R_{u_m}^{\text{EP}}$  and  $e_r \in E$  do
7:      $\mathbf{e} \leftarrow (\mathbf{e}, e_r); e_m \leftarrow e_r; u_m \leftarrow u_r$  where  $(u_m, u_r) = \psi(e_r)$ 
8:     Remove  $e_r$  from  $E$  // grow the right end of  $\mathbf{e}$ 
9:   end while
10:  while  $\exists (e_l, e_1) \in R_{u_0}^{\text{EP}}$  and  $e_l \in E$  do
11:     $\mathbf{e} \leftarrow (e_l, \mathbf{e}); e_1 \leftarrow e_l; u_0 \leftarrow u_l$  where  $(u_l, u_0) = \psi(e_l)$ 
12:    Remove  $e_l$  from  $E$  // grow the left end of  $\mathbf{e}$ 
13:  end while
14:  if  $u_m = u_0$  and  $(e_1, e_m) \in R_{u_0}^{\text{EP}}$  then
15:    Add  $\mathbf{e}$  to  $C_S$ 
16:  else
17:    Add  $\mathbf{e}$  to  $T_S$ 
18:  end if
19: end while

```

implies the distinctness of edges in \mathbf{e} , ensuring that \mathbf{e} is indeed a trail, cf. Definition 4.3. Also by Definition 4.3, the trail in line 15 is a circuit. Then post-condition (a) follows from the classification in lines 14–18 and the fact that, inside the outermost while loop, all edges in E have been visited. Post-condition (b) holds because lines 6, 10, 14 imply that each edge added to the trail or circuit satisfies the pairing condition.

□

For the interface graph in Fig. 2(a) and the edge pairing in (4.35), the output of Algorithm 1 is shown in the last two columns of Fig. 2(c). For the initial trail (e_8) , the two while loops in lines 6–13 are skipped and the condition at line 14 holds with $u_0 = u_m = v_2$ and $(e_8, e_8) \in R_{v_2}^{\text{EP}}$; thus (e_8) is added into C_S . For the initial trails (e_{10}) or (e_{11}) , the two while loops in lines 6–13 extend the trail to $\mathbf{e} = (e_{15}, e_{10}, e_{11}, e_{16})$ due to (4.35); however, the condition $(e_{15}, e_{16}) \in R_{v_7}^{\text{EP}}$ at line 14 does not hold, so the trail \mathbf{e} is added into T_S . Similarly, (e_{13}, e_{12}, e_{14}) in Fig. 2

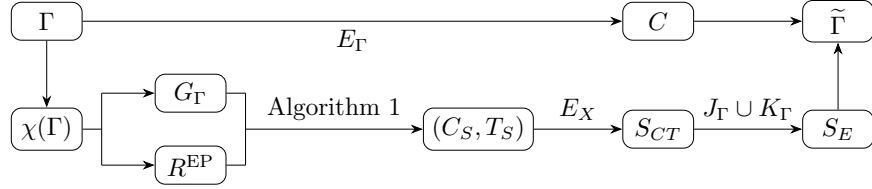


Fig. 3. The pipeline of constructing $\tilde{\Gamma}$ as a spline approximation of Γ , cf. Notation 4.26.

does not satisfy the pairing condition at line 14 and is also added into T_S .

The input parameter G of Algorithm 1 is not required to have the structure of an interface graph or even a planar graph; similarly, R^{EP} is not the smoothness indicator in Definition 4.23 but the edge pairing in Definition 4.22. Nonetheless, R^{EP} is *interpreted* as the smoothness indicator of the interface graph so that the output C_S and T_S correspond respectively to smooth closed curves approximated by periodic splines and to smooth curve segments approximated by not-a-knot splines. $C_S \cup T_S$ is not isomorphic to E_Γ and neither is C_S to C : circuits preserve smoothness in fitting splines while cycles represent the topology of each Yin set, cf. Definition 4.3. This discussion suggests the need for some set of splines isomorphic to $C_S \cup T_S$.

Definition 4.25. The *set of fitted splines*, written S_{CT} , is constructed by first concatenating marker sequences in E_X in (4.3) according to circuits or trails in $C_S \cup T_S$ and then interpolating each concatenated breakpoint sequence: a periodic spline for a circuit and a not-a-knot spline for a trail (that is not a circuit).

Cut S_{CT} at junctions and kinks and we obtain the spline edge set S_E in Definition 4.9. The isomorphisms $S_E \cong E_\Gamma$ and $R^{\text{EP}} \cong V_\Gamma$ lead to

Notation 4.26. Denote by $\tilde{\Gamma} := [(\psi_\Gamma, C), (S_E, R^{\text{EP}})]$ a *spline approximation* of the interface $\chi(\Gamma)$, where ψ_Γ is the incidence function of the interface graph G_Γ in Definition 4.7, C the cycle set in Notation 4.8, S_E the spline edge set in Definition 4.9, and R^{EP} the smoothness indicator in Definition 4.23.

Our design of the boundary representation of multiple Yin sets is concisely summarized in Fig. 3. By Theorem 2.2, each of the N_p Yin sets in \mathcal{M} is uniquely represented by a set $\Gamma_i = \{\Gamma_{i,j}\}$ of posets of oriented Jordan curves. After constructing the interface graph $G_\Gamma = (V_\Gamma, E_\Gamma, \psi_\Gamma)$ for $\chi(\Gamma)$, we express the topology of Γ by the incidence function ψ_Γ and the cycle set C . With the smoothness of the interface at V_Γ recorded in R^{EP} , Algorithm 1 decomposes E_Γ into (C_S, T_S) , which, together with the corresponding sequences of markers, yields a set S_{CT} of splines isomorphic to $C_S \cup T_S$. Since the edges in $C_S \cup T_S$ are pairwise distinct and cover all edges in E_Γ , the set S_E can be generated by cutting splines in S_{CT} at junctions and kinks.

5. Algorithms

To solve the multiphase IT problem in Definition 3.2, we evolve the static approximation of the initial condition $\mathcal{M}(t_0)$ over a finite time interval. To this end, we divide the interval into uniform time steps of size k , write $t_n = nk$, and denote by the superscript n a computed value of a variable at time t_n . For example, S_E^n denotes the spline edge set that approximates the geometry of $\Gamma(t_n)$.

Definition 5.1. A *MARS method* is an IT method of the form

$$\mathcal{M}^{n+1} := (\chi_{n+1} \circ \varphi_{t_n}^k \circ \psi_n) \mathcal{M}^n, \quad (5.1)$$

where $\mathcal{M}^n \in \mathbb{Y}$ is an approximation of $\mathcal{M}(t_n) \in \mathbb{Y}$, $\varphi_{t_n}^k : \mathbb{Y} \rightarrow \mathbb{Y}$ a fully discrete mapping operation that approximates the exact flow map in (3.3), $\psi_n : \mathbb{Y} \rightarrow \mathbb{Y}$ an augmentation operation at t_n to prepare \mathcal{M}^n for $\varphi_{t_n}^k$, and $\chi_{n+1} : \mathbb{Y} \rightarrow \mathbb{Y}$ an adjustment operation after the mapping $\varphi_{t_n}^k$.

5.1. The multiphase cubic MARS method for tracking three or more materials

To track three or more materials, we specialize the three operations in (5.1) to propose a cubic MARS method in Definition 5.7, the core of which is an ARMS strategy¹³ adapted to a single spline with junctions and kinks.

The approximating spline set S_{CT} in Definition 4.25 contains both periodic splines and not-a-knot splines. Significantly, Theorem 4.19 indicates that the error analysis of not-a-knot splines fundamentally differs from those of periodic splines – the coefficient c_0 depends on $\frac{1}{r_b}$, cf. (4.16), and is determined by six breakpoints within the neighborhoods of the two endpoints of the spline. In particular, if we don't handle the three breakpoints near the endpoints, then r_b might be very close to r in Definition 4.13. Hence the error term in (4.20) degrades from $O(h_L^4)$ to $O\left(\frac{h_L^4}{r}\right)$, which results in accuracy deterioration for not-a-knot splines when r is small (a scenario frequently observed in the numerical experiments, see Sec. 7).

To address the accuracy deterioration in not-a-knot splines, we propose Algorithm 2 incorporating the ARMS strategy. The objective of Algorithm 2 is to ensure a lower bound $r_b^* > 1$ for r_b .

Algorithm 2 consists of two main steps:

- (i) *Locating inserted marker q_1* (line 4): A bisection search is performed over the parametric interval $[l_0, l_1]$ of curve S to find q_1 satisfying

$$r_{\text{tiny}} h_L \leq \|q_1 - q_0\|_2 \leq \min \left(\frac{1}{2r_b^*} h_L, \frac{1}{1 + r_b^*} \|p_1 - q_0\|_2 \right), \quad (5.2)$$

where r_b^* and r_{tiny} are not independent parameters, their values constrain each other. We suggest using $r_b^* = \frac{3}{2}$ or a value close to it. The first inequality $r_{\text{tiny}} h_L \leq \|q_1 - q_0\|_2$ ensures the lower bound of the chordal length

Algorithm 2 : $\mathbf{q} = \text{adjustEnds}(l_0, l_1, S_\varphi, r_{\text{tiny}}, h_L, r_b^*)$

Input: An interval $[l_0, l_1]$; a function $S_\varphi : [l_0, l_1] \rightarrow \mathbb{R}^2$; regularity parameters (r_{tiny}, h_L) ; a desired lower bound r_b^* of r_b in (4.16).

Output: A marker sequence $\mathbf{q} := (q_i)_{i=0}^M$.

Pre-conditions: (a) $l_1 > l_0 \geq 0$, $r_b^* \in \left(1, \frac{1}{2r_{\text{tiny}}}\right)$, $r_{\text{tiny}} \in \left(0, \min(\frac{1}{6}, \frac{1}{2r_b^*})\right)$;
 (b) $p_0 := S_\varphi(l_0)$ and $p_1 := S_\varphi(l_1)$ satisfy $\|p_1 - p_0\|_2 > (1 + r_b^*)r_{\text{tiny}}h_L$;
 (c) S_φ is a continuous bijection.

Post-conditions: (a) $q_0 = p_0$, $q_M = p_1$, $\forall i = 1, \dots, M$, $q_i \in S := \{S_\varphi(l) \mid l \in [l_0, l_1]\}$;
 (b) $\forall i = 0, \dots, M-1$, $S_\varphi^{-1}(q_i) < S_\varphi^{-1}(q_{i+1})$;
 (c) $M \geq 2$ and the sequence \mathbf{q} is (r_{tiny}, h_L) -regular;
 (d) $r_b^*\|q_1 - q_0\|_2 \leq \|q_2 - q_1\|_2$.

```

1: Initialize  $\mathbf{q} \leftarrow \emptyset$ 
2: Initialize  $p_0 \leftarrow S_\varphi(l_0)$ ;  $p_1 \leftarrow S_\varphi(l_1)$ ;  $i \leftarrow 0$ 
3:  $q_i \leftarrow p_0$ ;  $\mathbf{q} \leftarrow (q_i)$ ;  $i \leftarrow i + 1$  // insert  $p_0$  to  $\mathbf{q}$  as  $q_0$ 
   // locate  $q_1$  between  $q_0$  and  $p_1$ 
4:  $l \leftarrow \text{BisectionSearch}(l_0, l_1, r_{\text{tiny}}h_L, \min\left(\frac{1}{2r_b^*}h_L, \frac{1}{1+r_b^*}\|p_1 - q_0\|_2\right), S_\varphi)$ 
5:  $q_i \leftarrow S_\varphi(l)$ ;  $\mathbf{q} \leftarrow (\mathbf{q}, q_i)$ ;  $i \leftarrow i + 1$ 
   // ensure maximum chordal length  $\leq h_L$ 
6: while  $\|p_1 - q_{i-1}\|_2 > h_L$  do
   // locate  $q_i$  between  $q_{i-1}$  and  $p_1$ 
7:    $l \leftarrow \text{BisectionSearch}(l, l_1, \frac{1}{2}h_L, \min(h_L, \frac{1}{2}\|p_1 - q_{i-1}\|_2), S_\varphi)$ 
8:    $q_i \leftarrow S_\varphi(l)$ ;  $\mathbf{q} \leftarrow (\mathbf{q}, q_i)$ ;  $i \leftarrow i + 1$ 
9: end while
10:  $q_i \leftarrow p_1$ ;  $\mathbf{q} \leftarrow (\mathbf{q}, q_i)$  // ensure that  $p_1$  is the last marker of  $\mathbf{q}$ 

```

11: **function:** $l = \text{BisectionSearch}(l_l, l_r, low, high, S_\varphi)$

Input: A parameter interval $[l_l, l_r]$; a value interval $[low, high]$; a function S_φ .

Output: A parameter l .

Pre-conditions: (a) $[low, high] \subset [0, \|S_\varphi(l_r) - S_\varphi(l_l)\|_2]$;
 (b) S_φ is a continuous bijection.

Post-conditions: $\|S_\varphi(l) - S_\varphi(l_l)\|_2 \in [low, high]$.

```

12:  $p_l \leftarrow S_\varphi(l_l)$ 
13:  $l \leftarrow \frac{l_l + l_r}{2}$ ;  $p_m \leftarrow S_\varphi(l)$ 
14: while  $\|p_m - p_l\|_2 \notin [low, high]$  do
15:   if  $\|p_m - p_l\|_2 < low$  then
16:      $l_l \leftarrow l$ 
17:   else
18:      $l_r \leftarrow l$ 
19:   end if
20:    $l \leftarrow \frac{l_l + l_r}{2}$ ;  $p_m \leftarrow S_\varphi(l)$ 
21: end while

```

between q_0 and q_1 . The second inequality $\|q_1 - q_0\|_2 \leq \frac{1}{2r_b^*}h_L$ guarantees the upper bound h_L while simultaneously providing a partial sufficient condition for post-condition (d) $r_b^*\|q_1 - q_0\|_2 \leq \|q_2 - q_1\|_2$. Finally, $\|q_1 - q_0\|_2 \leq \frac{1}{1+r_b^*}\|p_1 - q_0\|_2$ ensures that post-condition (d) holds even

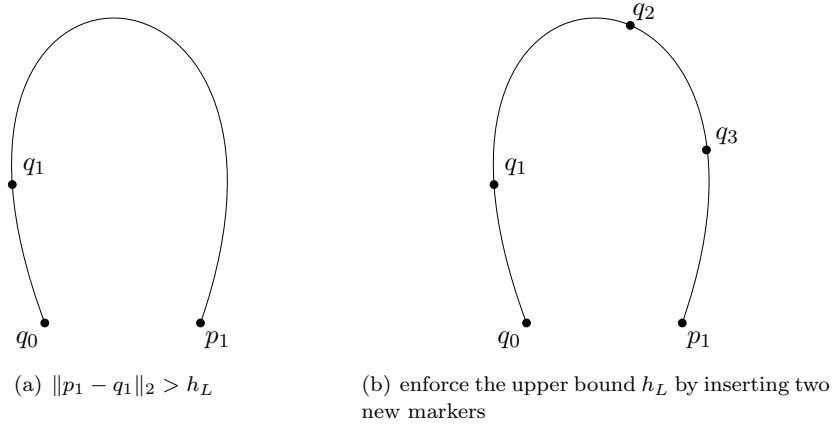


Fig. 4. The marker refinement between q_1 and p_1 in Algorithm 2.

when the loop in lines 6–9 is not entered.

- (ii) *Marker refinement* (lines 6–9): The distance from q_1 to p_1 may exceed the distance between endpoints p_0 and p_1 , as illustrated in Fig. 4(a). If $\|p_1 - q_1\|_2 > h_L$, intermediate markers are iteratively inserted within the parametric interval $[l, l_1]$ of curve S until the last inserted marker q_{i-1} satisfies $\|p_1 - q_{i-1}\|_2 \leq h_L$, as shown in Fig. 4(b). Each iteration locates a new insertion point q_i satisfying

$$\frac{1}{2}h_L \leq \|q_i - q_{i-1}\|_2 \leq \min\left(h_L, \frac{1}{2}\|p_1 - q_{i-1}\|_2\right) \quad (5.3)$$

by bisection search. The first inequality $\frac{1}{2}h_L \leq \|q_i - q_{i-1}\|_2$ ensures the lower bound $\frac{1}{2}h_L$ for the distance of adjacent inserted markers. Together with $\|q_1 - q_0\|_2 \leq \frac{1}{2r_b}h_L$ from (5.2), $\frac{1}{2}h_L \leq \|q_2 - q_1\|_2$ implies post-condition (d). The second inequality $\|q_i - q_{i-1}\|_2 \leq h_L$ enforces the upper bound h_L , while the last $\|q_i - q_{i-1}\|_2 \leq \frac{1}{2}\|p_1 - q_{i-1}\|_2$ provides a lower bound $\frac{1}{2}h_L$ for the distance between the final adjacent markers $q_M = p_1$ and q_{M-1} .

The following lemmas establish the correctness of Algorithm 2. The proof of Lemma 5.3 demonstrates that the design of (5.2) and (5.3) ensures the (r_{tiny}, h_L) -regularity of the marker sequence \mathbf{q} for not-a-knot splines as in Definition 4.17.

Lemma 5.2. *Function BisectionSearch in Algorithm 2 stops and its post-conditions hold.*

Proof. This follows directly from the intermediate value theorem. \square

Lemma 5.3. *Algorithm 2 stops and its post-conditions hold.*

Proof. The termination proof consists of two parts: the termination of the bisection search and the termination of the loop.

- (i) *Bisection search termination* (line 4): Lemma 5.2 and

$$0 < r_{\text{tiny}} h_L < \frac{1}{2r_b^*} h_L, \quad r_{\text{tiny}} h_L < \frac{1}{1+r_b^*} \|p_1 - q_0\|_2 < \|p_1 - q_0\|_2,$$

ensure the bisection search terminates under condition (5.2), where the first inequalities follow from pre-condition (a) and the second from pre-conditions (a) and (b).

- (ii) *Bisection search termination* (line 7): Given the loop condition $\|p_1 - q_{i-1}\|_2 > h_L$, we have

$$0 < \frac{1}{2} h_L < \min \left(h_L, \frac{1}{2} \|p_1 - q_{i-1}\|_2 \right) < \|p_1 - q_{i-1}\|_2. \quad (5.4)$$

Together with Lemma 5.2, the bisection search is guaranteed to terminate under condition (5.3).

- (iii) *Loop termination* (lines 6–9): Suppose for contradiction that the insertion process continues indefinitely. Let $\{q_i\}_{i=0}^N$ denote the sequence after inserting q_N . The cumulative chordal length is bounded by

$$\sum_{i=0}^{N-1} \|q_{i+1} - q_i\|_2 \leq L_S, \quad (5.5)$$

where $S = \{S_\varphi(l) \mid l \in [l_0, l_1]\}$ is the curve segment sequentially passing through all markers $\{q_i\}_{i=0}^N$ and L_S the total arc length of S . However, the condition $\|q_{i+1} - q_i\|_2 > \frac{1}{2} h_L$ from (5.3) implies $\sum_{i=0}^{N-1} \|q_{i+1} - q_i\|_2 > \frac{N-1}{2} h_L$, which contradicts the upper bound in (5.5). Thus the loop must terminate.

We have shown that the algorithm will always terminate. Next we will verify the post-conditions (a), (b), (c), and (d) sequentially:

- (a)(b) The insertion order in lines 3, 8, and 10 ensures the marker sequence \mathbf{q} starts at p_0 , ends at p_1 , and the corresponding parameters on S_φ are strictly increasing. Thus post-conditions (a) and (b) are satisfied.
- (c) (i) The first two points q_0, q_1 satisfy the (r_{tiny}, h_L) -regularity: The bisection termination condition (5.2) yields that the inserted marker q_1 (line 5) and its predecessor $q_0 = p_0$ (line 3) satisfy

$$r_{\text{tiny}} h_L \leq \|q_1 - q_0\|_2 \leq \frac{1}{2r_b^*} h_L < h_L. \quad (5.6)$$

- (ii) If the loop in lines 6–9 is not entered, q_1, q_2 satisfy the (r_{tiny}, h_L) -regularity: The bisection termination condition (5.2), the loop termination condition $\|p_1 - q_1\|_2 \leq h_L$ in line 6, and the triangle inequality

$\|q_2 - q_0\| \leq \|q_2 - q_1\|_2 + \|q_1 - q_0\|_2$ give that the inserted marker $q_2 = p_1$ (line 10), its predecessor q_1 (line 5), and $q_0 = p_0$ (line 3) satisfy

$$r_{\text{tiny}} h_L \leq r_b^* \|q_1 - q_0\|_2 \leq \|q_2 - q_1\|_2 \leq h_L. \quad (5.7)$$

- (iii) If the loop in lines 6–9 is entered, $\forall i = 2, \dots, M-1, q_i, q_{i-1}$ satisfy the (r_{tiny}, h_L) -regularity: The termination condition (5.3) ensures that the inserted marker q_i (line 8) and its predecessor q_{i-1} (line 5 or 8) satisfy

$$r_{\text{tiny}} h_L < \frac{1}{2} h_L \leq \|q_i - q_{i-1}\|_2 \leq h_L. \quad (5.8)$$

- (iv) If the loop in lines 6–9 is entered, q_M, q_{M-1} satisfy the (r_{tiny}, h_L) -regularity: The loop termination condition $\|p_1 - q_{M-1}\|_2 \leq h_L$ in line 6, together with condition (5.3), implies that the inserted marker $q_M = p_1$ (line 10) and its predecessor q_{M-1} (line 8) satisfy

$$r_{\text{tiny}} h_L < \frac{1}{2} h_L \leq \|q_{M-1} - q_{M-2}\|_2 \leq \|q_M - q_{M-1}\|_2 \leq h_L, \quad (5.9)$$

where the second inequality comes from (5.8), and the third from $\|q_{M-1} - q_{M-2}\|_2 \leq \frac{1}{2} \|q_M - q_{M-2}\|_2$ in (5.3) and the triangle inequality $\|q_M - q_{M-2}\|_2 \leq \|q_M - q_{M-1}\|_2 + \|q_{M-1} - q_{M-2}\|_2$.

Therefore, the sequence \mathbf{q} always satisfies the (r_{tiny}, h_L) -regularity condition, thus verifying post-condition (c).

- (d) The first two points in \mathbf{q} are $q_0 = p_0$ (line 3) and q_1 (line 5).
- (i) If the loop in lines 6–9 is entered, then q_2 is inserted in line 8. By (5.6) and (5.8), we derive

$$r_b^* \|q_1 - q_0\|_2 \leq \frac{1}{2} h_L \leq \|q_2 - q_1\|_2.$$

- (ii) If the loop in lines 6–9 is not entered, then $q_2 = p_1$ (line 10). According to (5.7), we have

$$r_b^* \|q_1 - q_0\|_2 \leq \|q_2 - q_1\|_2.$$

Both cases satisfy post-condition (d). \square

The following ARMS strategy provides an algorithm for tracking a single spline, including periodic and not-a-knot types. It serves as the solid foundation for tracking multiple materials.

Definition 5.4 (The ARMS strategy for a single spline). Given a discrete flow map $\varphi_{t_n}^k : \mathbb{Y} \rightarrow \mathbb{Y}$, a periodic or not-a-knot cubic spline \mathbf{s}^n whose breakpoint sequence $(X_i)_{i=0}^{N^n}$ is (r_{tiny}, h_L) -regular in the sense of Definition 4.13, and a subset $\mathbf{z}^n \subset (X_i)_{i=0}^{N^n}$ that characterizes \mathbf{s}^n , the *ARMS strategy* generates from $(\varphi_{t_n}^k, \mathbf{s}^n, \mathbf{z}^n)$ a pair $(\mathbf{s}^{n+1}, \mathbf{z}^{n+1})$, where \mathbf{z}^{n+1} is the set of characterizing breakpoints of \mathbf{s}^{n+1} .

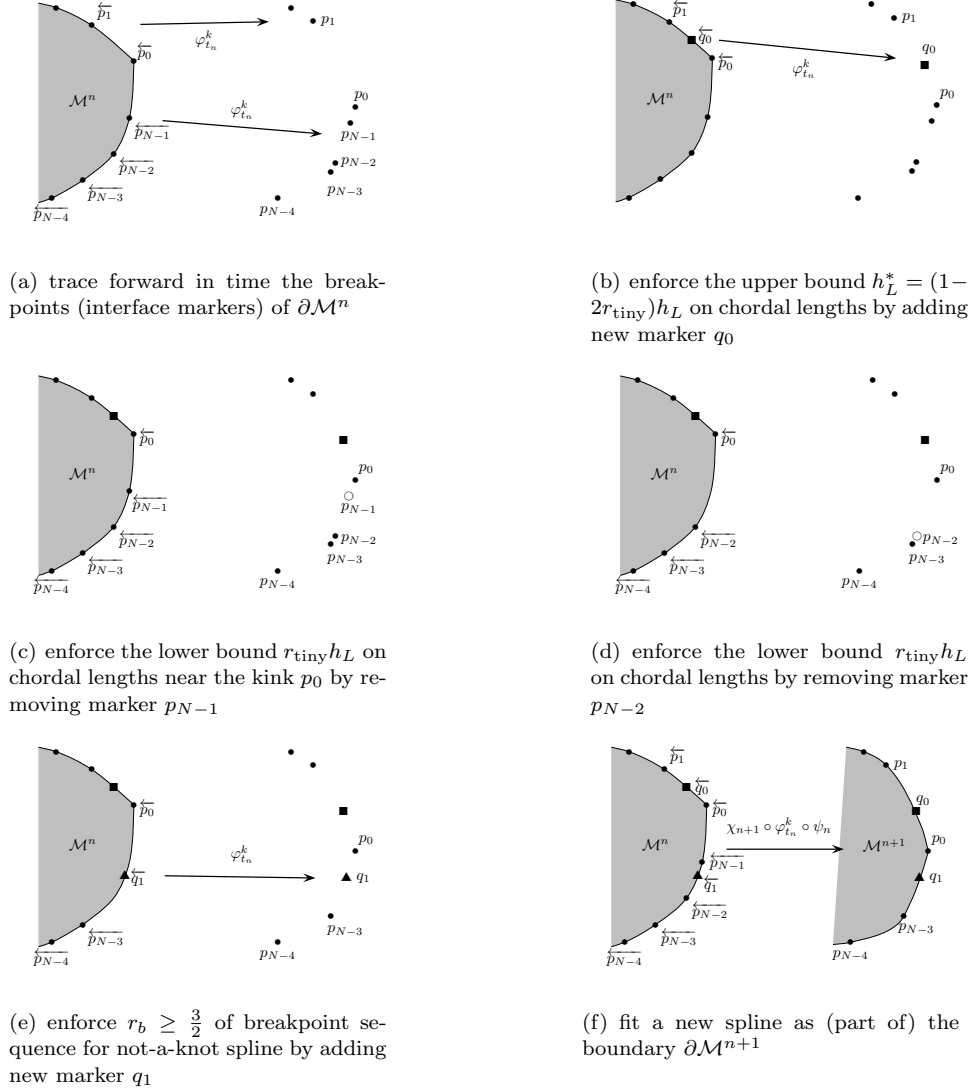
30 *Y. Tan & Y. Qian & Z. Li & Q. Zhang*

Fig. 5. The ARMS strategy. In subplot (a), the interface markers on $\partial\mathcal{M}^n$ are mapped to their images by the discrete flow map $\varphi_{t_n}^k$. In subplot (b), the distance between p_0 and p_1 is found to be larger than the upper bound h_L^* , a new marker q_0 (the solid square) is added and the new preimage sequence is mapped to time $t_n + k$ so that distances between both p_0, q and q, p_1 are smaller than h_L^* . In subplot (c), the distance between p_0 and p_{N-1} is found to be smaller than the lower bound $r_{\text{tiny}}h_L$ and p_0 is a kink, therefore, the marker p_{N-1} (the hollow circle) is removed. In subplot (d), the distance between p_{N-2} and p_{N-3} is smaller than $r_{\text{tiny}}h_L$, and the marker p_{N-2} is also removed. In subplot (e), the distance between p_0 and p_{N-3} is found to be larger than that between p_{N-3} and p_{N-4} , which implies $r_b < \frac{3}{2}$, thus a new marker q_1 (the solid triangle) is added and the new preimage sequence is mapped to time $t_n + k$ so that new markers satisfy $r_b \geq \frac{3}{2}$ for fitting a not-a-knot spline. In subplot (f), we obtain (part of) $\partial\mathcal{M}^{n+1}$ by fitting a new not-a-knot spline through the new chain of markers “ $p_0 \rightarrow q_0 \rightarrow p_1 \rightarrow \dots \rightarrow p_{N-4} \rightarrow p_{N-3} \rightarrow q_1 \rightarrow p_0$ ”.

- (ARMS-1) Initialize $(p_i)_{i=0}^{N^{n+1}}$ with $N^{n+1} \leftarrow N^n$ and $p_i \leftarrow \varphi_{t_n}^k(X_i)$; also set $\mathbf{z}^{n+1} = \varphi_{t_n}^k(\mathbf{z}^n)$.
- (ARMS-2) For a chordal length $\|p_j - p_{j+1}\|_2$ greater than $h_L^* := (1 - 2r_{\text{tiny}})h_L$,
- (a) locate $X_j = (x(l_j), y(l_j))$ and $X_{j+1} = (x(l_{j+1}), y(l_{j+1}))$ on \mathbf{s}^n as preimages of p_j and p_{j+1} ,
 - (b) divide the interval $[l_j, l_{j+1}]$ of parametrization into $\left\lceil \frac{\|p_j - p_{j+1}\|_2}{h_L^*} \right\rceil$ equidistant subintervals, compute the corresponding new markers on $\mathbf{s}^n(l)$, insert them in between X_j and X_{j+1} , and
 - (c) insert the images of new markers under $\varphi_{t_n}^k$ into the new sequence between p_j and p_{j+1} .
- Repeat (a, b, c) until no chordal length is greater than h_L^* .
- (ARMS-3) Remove chords of negligible lengths from the sequence $(p_i)_{i=0}^{N^{n+1}}$:
- (a) for each $p_j \in \mathbf{z}^{n+1}$, keep removing p_{j+1} from the breakpoint sequence until $\|p_j - p_{j+1}\|_2 \geq r_{\text{tiny}}h_L$ holds and keep removing p_{j-1} from the sequence until $\|p_j - p_{j-1}\|_2 \geq r_{\text{tiny}}h_L$ holds,
 - (b) locate a point $p_\ell \in (X_i)$ satisfying $\|p_\ell - p_{\ell+1}\|_2 < r_{\text{tiny}}h_L$ and set $j = \ell$,
 - (c) if $\|p_j - p_{j+1}\|_2 < r_{\text{tiny}}h_L$, keep removing p_{j+1} from the point sequence until $\|p_j - p_{j+1}\|_2 \geq r_{\text{tiny}}h_L$ holds for the new p_{j+1} ,
 - (d) increment j by 1 and repeat (b, c) until all chords have been checked.
- (ARMS-4) Construct spline \mathbf{s}^{n+1} from the breakpoint sequence $(p_i)_{i=0}^{N^{n+1}}$:
- (a) If \mathbf{s}^n is a periodic cubic spline, construct \mathbf{s}^{n+1} from the breakpoint sequence $(p_i)_{i=0}^{N^{n+1}}$ using the periodic condition.
 - (b) If $\mathbf{s}^n : [0, L^n] \rightarrow \mathbb{R}^2$ is a not-a-knot spline, define $S_\varphi := \varphi_{t_n}^k \circ \mathbf{s}^n$. For breakpoints p_0, p_1 , and p_2 , if $\frac{3}{2}\|p_1 - p_0\|_2 > \|p_2 - p_1\|_2$, keep removing p_1 from the breakpoint sequence until $\|p_1 - p_0\|_2 > \frac{5}{2}r_{\text{tiny}}h_L$ holds for some p_1 and then replace (p_0, p_1) by $\mathbf{q}_l \leftarrow \text{adjustEnds}(0, l_1, S_\varphi, r_{\text{tiny}}, h_L, \frac{3}{2})$ in Algorithm 2 with l_1 satisfying $p_1 = S_\varphi(l_1)$. For breakpoints $p_{N^{n+1}}, p_{N^{n+1}-1}$ and $p_{N^{n+1}-2}$, apply symmetric processing. Lastly, construct \mathbf{s}^{n+1} from the updated breakpoint sequence using the not-a-knot condition.

We have assumed cyclic indexing for periodic splines.

In this work, the characterization breakpoints in \mathbf{z}^0 are taken from the vertex set V_{Γ^0} of the interface graph G_{Γ^0} at the initial time t_0 . See Fig. 5 for an illustration of the ARMS strategy.

The ARMS strategy in Definition 5.4 embodies the main idea of MARS framework. In substeps (ARMS-2b) and (ARMS-4b), the augmentation operation ψ_n adds new markers on $\partial\mathcal{M}^n$ to impose an upper bound for adjacent mapped marker spacing. The discrete flow map $\varphi_{t_n}^k$ advances the interface markers on $\partial\mathcal{M}^n$ to

time $t_n + k$, specifically implemented in step (ARMS-1), substeps (ARMS-2c) and (ARMS-4b). The adjustment operation χ_{n+1} removes marker images on $\partial\mathcal{M}^{n+1}$ to enforce the lower bound $r_{\text{tiny}}h_L$ through step (ARMS-3) and substep (ARMS-4b). Finally, substep (ARMS-4b) adjusts the breakpoint sequence of not-a-knot splines by taking $r_b^* = \frac{3}{2}$ in Algorithm 2 to ensure the lower bound of r_b .

Lemma 5.5. *If $r_{\text{tiny}} < \frac{1}{6}$, the breakpoint sequence $(p_i)_{i=0}^{N^{n+1}}$ of \mathbf{s}^{n+1} is (r_{tiny}, h_L) -regular for both periodic and not-a-knot splines.*

Proof. Lemma 5.3 demonstrates that substep (ARMS-4b) ensures the (r_{tiny}, h_L) -regularity of the breakpoint sequence as in Definition 4.17 for not-a-knot splines. Hence it suffices to show that the breakpoint sequence $(p_i)_{i=0}^{N^{n+1}}$ satisfies the (r_{tiny}, h_L) -regularity before (ARMS-4).

(ARMS-2) ensures that no chordal length is greater than h_L^* before (ARMS-3). Considering that the characterizing breakpoint set \mathbf{z}^{n+1} is non-empty, then substep (ARMS-3a) removes marker images near \mathbf{z}^{n+1} and the maximum length of any new chord is increased to $h_L^* + r_{\text{tiny}}h_L$; see Fig. 5(c). Subsequently, as illustrated in Fig. 5(d), sequential point removal in substeps (ARMS-3b,c,d) further relaxes the maximum length to

$$h_L^* + r_{\text{tiny}}h_L + r_{\text{tiny}}h_L = h_L,$$

which, together with the fact that (ARMS-3) enforces a lower bound of $r_{\text{tiny}}h_L$ on chordal lengths, completes the proof. \square

In light of Lemma 5.5, the (r_{tiny}, h_L) -regularity are maintained as *representation invariants* throughout our algorithms of evolving the interface.

Remark 5.6. The ARMS strategy in Definition 5.4 are different from that in Ref. 13 in three aspects:

- (1) We take $h_L^* = (1 - 2r_{\text{tiny}})h_L$ to maintain the (r_{tiny}, h_L) -regularity instead of $(1 - r_{\text{tiny}})h_L$ in Ref. 13. In addition, the condition $r_{\text{tiny}} < \frac{1}{6}$ implies $r_{\text{tiny}}h_L < \frac{1}{2}h_L^*$, thus avoiding additional operations.
- (2) As established in the motivational discussion, the fundamental distinction in error analysis between not-a-knot splines and periodic splines requires systematic modification of the boundary condition constant r_b before fitting not-a-knot splines. Therefore, in substep (ARMS-4b), Algorithm 2 is applied to both boundary breakpoint sets to enforce a lower bound on r_b before the construction of the spline \mathbf{s}^{n+1} . Additionally, this ensures the (r_{tiny}, h_L) -regularity of the breakpoint sequence for not-a-knot splines.
- (3) Since not-a-knot splines are not necessarily closed and the MARS method is defined on Yin sets, the ARMS strategy for a single spline in Definition 5.4 might not constitute a MARS method. In contrast, the ARMS strategy in Ref. 13 with the fully discrete flow map indeed combine to a MARS

method. To resolve this discrepancy, we propose the cubic MARS method for multiple materials.

Definition 5.7 (The multiphase cubic MARS method). Given a discrete flow map $\varphi_{t_n}^k$ that approximates a homeomorphic flow map ϕ , a spline approximation $\tilde{\Gamma}^0 = [(\psi_\Gamma, C), (S_E^0, R^{\text{EP}})]$ of the initial condition $\mathcal{M}(t_0)$ in Notation 4.26, and a pair (S_{CT}^0, Z_{CT}^0) where $S_{CT}^0 \cong (C_S \cup T_S)$ is the set of fitted splines in Definition 4.25 and the function $Z_{CT}^0 : S_{CT}^0 \rightarrow 2^{V_{\Gamma^0}}$ given by $Z_{CT}^0(\mathbf{s}) = \mathbf{s} \cap V_{\Gamma^0}$ maps the spline \mathbf{s} to a subset of V_{Γ^0} , the multiphase cubic MARS method for the IT problem in Definition 3.2 advances (S_{CT}^n, Z_{CT}^n) to $(S_{CT}^{n+1}, Z_{CT}^{n+1})$ as follows.

- (a) For each spline $\mathbf{s}^n \in S_{CT}^n$ and its characterization set $\mathbf{z}^n = Z_{CT}^n(\mathbf{s}^n)$, obtain $\mathbf{s}^{n+1} \in S_{CT}^{n+1}$ and \mathbf{z}^{n+1} by applying the ARMS strategy in Definition 5.4 to $(\varphi_{t_n}^k, \mathbf{s}^n, \mathbf{z}^n)$. All pairs in $\{(\mathbf{s}^{n+1}, \mathbf{z}^{n+1}) : \mathbf{s}^{n+1} \in S_{CT}^{n+1}\}$ constitute Z_{CT}^{n+1} .
- (b) (optional) Assemble $\tilde{\Gamma}^{n+1}$ by first converting S_{CT}^{n+1} to S_E^{n+1} and then combining the cycle set C with S_E^{n+1} ; see the second half of Fig. 3.
- (c) (optional) Compute, for a main flow solver, the intersection of control volumes to each phase \mathcal{M}_i^{n+1} via the Boolean algebra in Theorem 2.3.

For optimal efficiency, the evolutionary variable in Definition 5.7 is designed to be S_{CT}^n instead of $\tilde{\Gamma}^n$. Step (b) in Definition 5.7 is optional because $\tilde{\Gamma}^{n+1}$ is not needed in evolving the interface $\Gamma(t)$; on the other hand, an IT method is responsible for coming up with an approximation of $\Gamma(t)$. Step (c) is also optional for similar reasons.

The multiphase cubic MARS method can be extended to the case of the exact flow map in Definition 4.25 being not homeomorphic, via checking intersections of the edges of the interface graph and duely updating the topology of the tracked phases. We defer to a future paper the details for handling topological changes.

Although the Lagrangian grid of moving markers suffices to evolve the interface, an Eulerian grid is needed to couple an IT method with a main flow solver. Assuming for simplicity that the Eulerian grid has a uniform size h along each dimension, we specify $h_L = O(h^\alpha)$ to connect the length scale of the interface to the length scale of the bulk flow. Since the interface is a set of codimension one and a simulation has $O(\frac{1}{h})$ time steps, the complexity of a MARS method with $h_L = O(h^\alpha)$ is $O(\frac{1}{h^{1+\alpha}})$. In contrast, the optimal complexity of a main flow solver is $O(\frac{1}{h^3})$ in two dimensions. Therefore, a MARS method with $\alpha \leq 2$ does not increase the complexity of the entire solver; see [26, Sec. 5.2.4] for more discussions.

5.2. A curvature-based ARMS strategy

With a constant h_L specified in the ARMS strategy, the cubic MARS method performs well in most cases. However, for IT problems with very large variations of interface curvature, the limited range of $[r_{\text{tiny}}, 1]$ might result in large errors at high-curvature arcs and small errors at low-curvature ones, deteriorating the accuracy and efficiency.

This problem can be overcome by further varying h_L according to the local curvature κ of the deforming interface so that arcs with high curvature have a dense distribution of markers.¹³ In this work, we set h_L to a continuous function that is monotonically increasing with respect to the *radius of curvature* $\rho := \frac{1}{|\kappa|}$,

$$h_L(\rho) := \begin{cases} r_{\min} h_L^c & \text{if } \rho \leq \rho_{\min}; \\ r_{\min} h_L^c + (1 - r_{\min}) h_L^c \cdot \sigma^c \left(\frac{\rho - \rho_{\min}}{\rho_{\max} - \rho_{\min}} \right) & \text{if } \rho_{\min} < \rho < \rho_{\max}; \\ h_L^c & \text{if } \rho \geq \rho_{\max}, \end{cases} \quad (5.10a)$$

$$r_{\min} := \max \left(r_{\min}^c, \frac{\rho_{\min}}{\rho_{\max}} \right); \quad (5.10b)$$

$$\rho_{\min} := \max(\rho_{\min}^c, \min_i \rho_i), \quad \rho_{\max} := \min(\rho_{\max}^c, \max_i \rho_i), \quad (5.10c)$$

where the user-specified constants ρ_{\max}^c and ρ_{\min}^c remove the distractions of linear segments and very-high-curvature markers, respectively, and $r_{\min}^c \in (0, 1]$ controls the condition number of spline fitting in that the *highest possible ratio of the longest chordal length over the shortest one* is $R_{\max} := \frac{1}{r_{\min}^c r_{\text{tiny}}}$. Note that R_{\max} would be $\frac{\rho_{\max}^c}{\rho_{\min}^c r_{\text{tiny}}}$ if r_{\min} were defined as $\frac{\rho_{\min}}{\rho_{\max}}$. If the fitted spline is \mathcal{C}^2 at the i th marker X_i , we calculate ρ_i as the radius of curvature of the spline at X_i ; otherwise we compute the two radii ρ_i^\pm by one-sided differentiation of piecewise polynomials at the two sides of X_i . The continuous bijection $\sigma^c : [0, 1] \rightarrow [0, 1]$ must satisfy $\sigma^c(0) = 0$ and $\sigma^c(1) = 1$.

We refer to (5.10) as the *curvature-based formula for the maximum chordal length*. To harness its flexibility, the user needs to specify, for the problem at hand, all values of $\rho_{\min}^c, \rho_{\max}^c, h_L^c, r_{\min}^c$, and the form of σ^c such as $\sigma^c(x) = x$. In contrast, $r_{\min}^c r_{\text{tiny}}$ is the *infimum of chordal-length ratios*.

Suppose a line segment has its initial marker density at $\frac{1}{h_L^c}$ and its curvature is increasing. Then (5.10) dictates that more markers will be added to the arc, increasing the marker density up to $\frac{1}{r_{\min}^c h_L^c}$. If the markers on the arc are also squeezed by the flow map, then the (r_{tiny}, h_L) -regularity in Definition 5.4 implies that the marker density can be further increased up to $\frac{1}{r_{\text{tiny}} r_{\min}^c h_L^c}$. Therefore, the maximum increase ratio of the marker density of a line segment is R_{\max} . By similar arguments, the maximum decrease ratio of the marker density of a high-curvature arc is also R_{\max} . These discussions are helpful for selecting values of the parameters with the c superscript.

6. Analysis

The volume of a Yin set \mathcal{Y} is given by

$$\|\mathcal{Y}\| := \left| \int_{\mathcal{Y}} d\mathbf{x} \right|, \quad (6.1)$$

where the integral can be interpreted as a Riemann integral since \mathcal{Y} is semianalytic. The regularized symmetric difference $\oplus : \mathbb{Y} \times \mathbb{Y} \rightarrow \mathbb{Y}$ is defined as

$$\mathcal{P} \oplus \mathcal{Q} := (\mathcal{P} \setminus \mathcal{Q}) \cup^{\perp\perp} (\mathcal{Q} \setminus \mathcal{P}), \quad (6.2)$$

which satisfies

$$\forall \mathcal{Y} \in \mathbb{Y}, \quad \mathcal{Y} \oplus \mathcal{Y} = \emptyset, \quad \emptyset \oplus \mathcal{Y} = \mathcal{Y}; \quad (6.3)$$

$$\forall \mathcal{P}, \mathcal{Q} \in \mathbb{Y}, \quad \|\mathcal{P} \oplus \mathcal{Q}\| \leq \|\mathcal{P}\| + \|\mathcal{Q}\|. \quad (6.4)$$

It follows from (6.1), (6.2), (6.3) and (6.4) that (\mathbb{Y}, d) forms a metric space where the metric $d : \mathbb{Y} \times \mathbb{Y} \rightarrow [0, +\infty)$ is

$$\forall \mathcal{P}, \mathcal{Q} \in \mathbb{Y}, \quad d(\mathcal{P}, \mathcal{Q}) := \|\mathcal{P} \oplus \mathcal{Q}\|. \quad (6.5)$$

6.1. IT errors of a MARS method

In light of (6.5), the IT error of a MARS method at time t_n is defined as

$$E_{\text{IT}}(t_n) := \|\mathcal{M}(t_n) \oplus \mathcal{M}^n\|. \quad (6.6)$$

Definition 6.1. Individual IT errors of a MARS method include the following.

- The representation error E^{REP} is the error caused by approximating the initial Yin set $\mathcal{M}(t_0)$ with a discrete representation \mathcal{M}^0 .
- The augmentation error $E^{\text{AUG}}(t_n)$ is the accumulated error of augmenting the Yin sets by ψ_j .
- The mapping error $E^{\text{MAP}}(t_n)$ is the accumulated error of approximating the exact flow map ϕ with the discrete flow map $\varphi_{t_j}^k$.
- The adjustment error $E^{\text{ADJ}}(t_n)$ is the accumulated error of adjusting the mapped Yin sets by χ_{j+1} .

More precisely, these individual errors at $t_n = t_0 + nk$ are defined as:

$$E^{\text{REP}}(t_n) = \|\phi_{t_0}^{nk} [\mathcal{M}(t_0), \mathcal{M}^0]\|; \quad (6.7a)$$

$$E^{\text{AUG}}(t_n) = \left\| \bigoplus_{j=0}^{n-1} \phi_{t_j}^{(n-j)k} [\mathcal{M}_{\psi}^j, \mathcal{M}^j] \right\|; \quad (6.7b)$$

$$E^{\text{MAP}}(t_n) = \left\| \bigoplus_{j=1}^n \phi_{t_j}^{(n-j)k} [\phi_{t_{j-1}}^k \mathcal{M}_{\psi}^{j-1}, \varphi_{t_{j-1}}^k \mathcal{M}_{\psi}^{j-1}] \right\|; \quad (6.7c)$$

$$E^{\text{ADJ}}(t_n) = \left\| \bigoplus_{j=1}^n \phi_{t_j}^{(n-j)k} [\varphi_{t_{j-1}}^k \mathcal{M}_{\psi}^{j-1}, \mathcal{M}^j] \right\|. \quad (6.7d)$$

where $\mathcal{M}_{\psi}^j := \psi_j \mathcal{M}^j$ and $\phi_{t_j}^{(n-j)k} [\cdot, \cdot]$ is a shorthand notation given by

$$\forall \mathcal{P}, \mathcal{Q} \in \mathbb{Y}, \quad \phi_{t_0}^{\tau} [\mathcal{P}, \mathcal{Q}] := \phi_{t_0}^{\tau} (\mathcal{P}) \oplus \phi_{t_0}^{\tau} (\mathcal{Q}). \quad (6.8)$$

The IT error of a MARS method is bounded by the sum of the individual errors in (6.7).

Theorem 6.2. *For a single phase, the IT errors of a MARS method satisfy*

$$E_{\text{IT}}(t_n) \leq E^{\text{REP}}(t_n) + E^{\text{AUG}}(t_n) + E^{\text{MAP}}(t_n) + E^{\text{ADJ}}(t_n). \quad (6.9)$$

Proof. See [13, Theorem 3.3]. \square

6.2. The representation error E^{REP}

By Sec. 4.1, all topological structures of the initial condition $\partial\mathcal{M}(t_0)$ have been captured in the interface graph. By Theorems 4.12 and 4.19 in Sec. 4.2, the geometry of $\chi(\Gamma) = \partial\mathcal{M}(t_0)$ has been approximated by $\partial\mathcal{M}^0$ to fourth-order accurate by periodic and not-a-knot cubic splines. More precisely, $\partial\mathcal{M}^0$ is homeomorphic to $\partial\mathcal{M}(t_0)$ and the distance between corresponding points on $\partial\mathcal{M}^0$ and $\partial\mathcal{M}(t_0)$ is $O(h_L^4)$. Therefore, we have

$$E^{\text{REP}}(t_n) = \left\| \phi_{t_0}^{nk} [\mathcal{M}(t_0), \mathcal{M}^0] \right\| = O(h_L^4), \quad (6.10)$$

where the first equality follows from (6.7a) and the second from

Lemma 6.3. *Suppose $\Upsilon : \partial\mathcal{P} \rightarrow \partial\mathcal{Q}$ is a homeomorphism between two Yin sets \mathcal{P}, \mathcal{Q} such that $\max_{\mathbf{X} \in \partial\mathcal{P}} \|\mathbf{X} - \Upsilon(\mathbf{X})\|_2 = \epsilon$. Then $\|\phi_{t_0}^T[\mathcal{P}, \mathcal{Q}]\| = O(\epsilon)$.*

Proof. See that of [13, Lemma 5.4]. \square

6.3. The augmentation error E^{AUG}

By Definition 5.4, the augmentation operation consists of adding markers on $\partial\mathcal{M}^j$ in (ARMS-2) to enforce the upper bound h_L of chordal length or in (ARMS-4) to ensure good conditioning of the not-a-knot splines. Since the added markers are on $\partial\mathcal{M}^j$, the spline $\partial\mathcal{M}^j$ satisfies all constraints of $\partial\mathcal{M}_{\psi}^j$, which implies that the two splines $\partial\mathcal{M}_{\psi}^j$ and $\partial\mathcal{M}^j$ are exactly the same. Hence (6.3) yields $\|\mathcal{M}_{\psi}^j \oplus \mathcal{M}^j\| = 0$, and consequently (6.7b) implies

$$E^{\text{AUG}}(t_n) = \left\| \bigoplus_{j=0}^{n-1} \phi_{t_j}^{(n-j)k} [\mathcal{M}_{\psi}^j, \mathcal{M}^j] \right\| = 0. \quad (6.11)$$

6.4. The mapping error E^{MAP}

The analysis of E^{MAP} entails the comparison of the fully discrete flow map φ with the exact flow map ϕ . By (6.7c), it is essential to estimate the mapping error within a single time step. The key challenge lies in estimating

$$\epsilon_j^{\text{MAP}} := \max_{\mathbf{X} \in \partial\mathcal{M}_{\psi}^{j-1}} \left\| \phi_{t_{j-1}}^k \mathbf{X} - \varphi_{t_{j-1}}^k \mathbf{X} \right\|_2 \quad (6.12)$$

since Lemma 6.3 implies $E^{\text{MAP}}(t_n) = \sum_{j=1}^n O(\epsilon_j^{\text{MAP}})$.

The first step of estimating ϵ_j^{MAP} is

Definition 6.4. A *semidiscrete flow map* is a function $\phi : \mathbb{Y} \rightarrow \mathbb{Y}$ that results from discretizing the exact flow map ϕ in time by a κ th-order ODE solver.

Suppose a Runge-Kutta method is employed to discretize ϕ . Then the semidiscrete flow map ϕ for the ODE (3.1) is of the form

$$\phi_0^k(\mathbf{X}^0) := \mathbf{X}^0 + k \sum_{j=1}^{n_{\text{stage}}} b_j \mathbf{y}_j \text{ where } \mathbf{y}_i = \mathbf{u} \left(\mathbf{X}^0 + k \sum_{j=1}^{n_{\text{stage}}} a_{ij} \mathbf{y}_j, t^0 + c_i k \right), \quad (6.13)$$

where a_{ij}, b_j, c_i constitute the standard Butcher tableau.

In the second step, we split ϵ_j^{MAP} into

$$\begin{cases} \epsilon_j^{\text{time}} := \max_{\mathbf{X} \in \partial \mathcal{M}_\psi^{j-1}} \left\| \phi_{t_{j-1}}^k \mathbf{X} - \phi_{t_{j-1}}^0 \mathbf{X} \right\|_2; \\ \epsilon_j^{\text{space}} := \max_{\mathbf{X} \in \partial \mathcal{M}_\psi^{j-1}} \left\| \phi_{t_{j-1}}^0 \mathbf{X} - \varphi_{t_{j-1}}^k \mathbf{X} \right\|_2, \end{cases} \quad (6.14)$$

where $\epsilon_j^{\text{time}} = O(k^{\kappa+1})$ follows directly from Definition 6.4 and the fact that ϕ acts on *all* points in $\partial \mathcal{M}_\psi^{j-1}$.

In the third step, we estimate $\epsilon_j^{\text{space}}$ in

Lemma 6.5. Suppose each piecewise smooth curve in $\partial \mathcal{M}_\psi^{j-1}$ is approximated by a periodic or not-a-knot cubic spline as discussed in Sec. 4. Then

$$\epsilon_j^{\text{space}} = O(kh_L^4). \quad (6.15)$$

Proof. By (6.14), $\epsilon_j^{\text{space}} = \max_{p(x) \in \partial \mathcal{M}_\psi^{j-1}} \left\| \phi_{t_{j-1}}^k p(x) - \varphi_{t_{j-1}}^k p(x) \right\|_2$. According to Definition 6.4, $\phi_{t_{j-1}}^k$ acts on all points in $\partial \mathcal{M}_\psi^{j-1}$, and thus $\partial \left(\phi_{t_{j-1}}^k \mathcal{M}_\psi^{j-1} \right)$ might not be a cubic spline. In contrast, we know from Definition 5.4 that $\varphi_{t_{j-1}}^k$ only acts on the markers of $\partial \mathcal{M}_\psi^{j-1}$, the images of which are then used to construct cubic splines.

Denote by $l \in [l_0, l_N]$ the corresponding cumulative chordal length of the markers on $\partial \left(\phi_{t_{j-1}}^k \mathcal{M}_\psi^{j-1} \right)$ and let $\mathbf{S} : [l_0, l_N] \rightarrow \mathbb{R}^2$ be the spline fitted through these markers. Let $\mathbf{F} : [l_0, l_N] \rightarrow \mathbb{R}^2$ be the functional form of the curve $\partial \left(\phi_{t_{j-1}}^k \mathcal{M}_\psi^{j-1} \right)$. Then, we have

$$\epsilon_j^{\text{space}} = \max_l \left\| \mathbf{F}(l) - \mathbf{S}(l) \right\|_2 \leq c_0 h_L^4 \max_{\xi \in [l_0, l_N] \setminus X_b} \left| \mathbf{F}^{(4)}(\xi) \right| = O(kh_L^4).$$

where the second step follows from Theorems 4.12 and 4.19 and the last from $\mathbf{F}^{(4)}(\xi) = O(k)$, an implication of Lemma 6.6. \square

Lemma 6.6. Let $\mathbf{p} : [0, \tilde{l}_N] \rightarrow \mathbb{R}^2$ be a periodic or not-a-knot cubic spline fitted through a sequence $(\mathbf{X}_i^0)_{i=0}^N$ of breakpoints with \tilde{l}_i 's as the cumulative chordal lengths.

38 *Y. Tan & Y. Qian & Z. Li & Q. Zhang*

Denote by $\Gamma(t)$ the loci of \mathbf{p} at time $t \in [0, k]$ under the action of a semidiscrete flow map ϕ . Then we have

$$\forall \mathbf{X} \in \Gamma(k) \setminus \left\{ \phi_0^k(\mathbf{X}_i^0) : i = 0, \dots, N \right\}, \quad \frac{d^4 \mathbf{X}(l)}{dl^4} = O(k), \quad (6.16)$$

where l is the cumulative chordal length determined from the breakpoint sequence (\mathbf{X}^k) where $(\mathbf{X}^t) := \left(\phi_0^t(\mathbf{X}_i^0) \right)_{i=0}^N$.

Proof. At any time $t \in [0, k]$, the curve $\Gamma(t)$ is parametrized by l , the cumulative chordal length of the sequence (\mathbf{X}^t) . For any sufficiently small k , $\Gamma(t)(l)$ is homeomorphic to $\mathbf{p}(\tilde{l})$; in particular, $\Gamma(0) = \mathbf{p}$. Therefore, for any $t \in (0, k]$, there exists a bijective affine transformation that relates l to \tilde{l} and vice versa. Hence $\frac{d\tilde{l}}{dl}$ is a nonzero constant and $\frac{d^2 \tilde{l}}{dl^2} = 0$. By (6.13), we have

$$\forall \mathbf{X} \in \Gamma(k), \exists \mathbf{X}^0 \in \mathbf{p}, \text{ s.t. } \mathbf{X} = \phi_0^k(\mathbf{X}^0) = \mathbf{X}^0 + k \sum_{j=1}^{n_{\text{stage}}} b_j \mathbf{y}_j, \quad (6.17)$$

where $\mathbf{y}_i = \mathbf{u}(\mathbf{X}^0 + k \sum_{j=1}^{n_{\text{stage}}} a_{ij} \mathbf{y}_j, t^0 + c_i k)$. The fourth derivative of (6.17) at any $\mathbf{X} \notin \left\{ \phi_0^k(\mathbf{X}_i^0) : i = 0, \dots, N \right\}$, the chain rule, and $\frac{d^2 \tilde{l}}{dl^2} = 0$ yield

$$\frac{d^4 \mathbf{X}(l)}{dl^4} = \frac{d^4 \mathbf{X}^0}{d\tilde{l}^4} \left(\frac{d\tilde{l}}{dl} \right)^4 + k \sum_{j=1}^{n_{\text{stage}}} b_j \frac{d^4 \mathbf{u}}{d\tilde{l}^4} + O(k^2).$$

Then the proof is completed by $\frac{d^4 \mathbf{X}^0}{d\tilde{l}^4} \equiv 0$, i.e., the fourth derivative of any cubic polynomial vanishes. \square

6.5. The adjustment error E^{ADJ}

Consider a smooth curve $\partial \mathcal{M}_S^j$ that interpolates all markers of $\partial \varphi_{t_{j-1}}^k \mathcal{M}_\psi^{j-1}$ and $\partial \mathcal{M}^j$, the cubic splines immediately before and after performing the adjustment operation (ARMS-3), respectively. Both splines can be considered as approximations of the smooth curve $\partial \mathcal{M}_S^j$. By Theorem 4.12 and 4.19, the approximation error between corresponding points is $O(h_L^4)$. Therefore, removing a marker can be regarded as performing an $O(h_L^4)$ perturbation to that point and reconstructing the spline^a, and marker sequence of $\partial \varphi_{t_{j-1}}^k \mathcal{M}_\psi^{j-1}$ indeed satisfy the (r, h_L) -regularity for some $0 < r < r_{\text{tiny}}$ with sufficiently small k . Then Lemma 4.20, Lemma 6.3 together with the fact that the error on $[l_{i-1}, l_{i+1}]$ around the perturbed breakpoint \mathbf{X}_i is always $O(h_L) \cdot O(h_L^4) = O(h_L^5)$ imply

$$\left\| \phi_{t_j}^{(n-j)k} [\varphi_{t_{j-1}}^k \mathcal{M}_\psi^{j-1}, \mathcal{M}^j] \right\| = N_r^{j-1} \cdot O(h_L^5), \quad (6.18)$$

where N_r^j denotes the number of markers to be removed within $[t_j, t_{j+1}]$. Though N_r^j at each time step is difficult to control, Lemma 6.8 demonstrates that the total

^aAccording to the uniqueness of solution to the linear system, the spline reconstructed after perturbation is exactly the same as that fitted after removing markers, as analyzed in the augmentation error.

number of removing markers throughout the interface tracking remains $O\left(\frac{1}{h_L}\right)$, i.e.,

$$N_r := \sum_{j=0}^{T/k-1} N_r^j = O\left(\frac{1}{h_L}\right). \quad (6.19)$$

For a periodic or not-a-knot cubic spline with breakpoint sequence $(X_i)_{i=0}^{N^j}$ at t_j , we define a total variation to characterizes the interface:

$$V^j = \sum_{i=0}^{N^j-1} \left| \|X_{i+1} - X_i\|_2 - \frac{1}{3}h_L \right|. \quad (6.20)$$

The sequence $(X_i)_{i=0}^{N^j}$ will be close to a uniform distribution with a distance of $\frac{1}{3}h_L$ if the total variation approaches zero.

Lemma 6.7. *For a periodic or not-a-knot cubic spline whose breakpoint sequence $(X_i)_{i=0}^{N^j}$ is (r_{tiny}, h_L) -regular at t_j , if $0 < r_{\text{tiny}} < \frac{1}{6}$, then*

- (a) *The total variation at t_j is bounded, i.e., $V^j = O(1)$;*
- (b) *$\varphi_{t_j}^k$ changes V^j by $O(k)$;*
- (c) *Adding a marker in ψ_j reduces V^j by $\frac{1}{3}h_L + O(h_L^2) + O(kh_L)$;*
- (d) *V^j always decreases under χ_{j+1} ,*

where the augmentation operation ψ_j , the fully discrete mapping operation $\varphi_{t_j}^k$ and the adjustment operation χ_{j+1} are defined in Definition 5.1.

Proof. The condition $r_{\text{tiny}} < \frac{1}{6}$ implies

$$2r_{\text{tiny}}h_L < \frac{1}{3}h_L < \frac{1}{2}h_L^*, \quad (6.21)$$

where $h_L^* = (1 - 2r_{\text{tiny}})h_L$ is defined in (ARMS-2). We show (a), (b), (c), and (d) respectively.

For (a), ϕ is a diffeomorphic flow map implies that the total arc length of the cubic spline at t_j is always $O(1)$. Then the number of markers satisfies

$$N^j \leq \frac{L_{\partial\mathcal{M}^j}}{r_{\text{tiny}}h_L} = O\left(\frac{1}{h_L}\right), \quad (6.22)$$

where the first inequality comes from the (r_{tiny}, h_L) -regularity of the sequence $(X_i)_{i=0}^{N^j}$. Hence

$$V^j = \sum_{i=0}^{N^j-1} \left| \|X_{i+1} - X_i\|_2 - \frac{1}{3}h_L \right| \leq N^j \cdot \frac{2}{3}h_L = O(1).$$

40 *Y. Tan & Y. Qian & Z. Li & Q. Zhang*

For (b), write $p_i = \varphi_{t_j}^k(X_i)$ and L the Lipschitz constant of \mathbf{u} , then

$$\begin{aligned} & \|p_{i+1} - p_i\|_2 - \|X_{i+1} - X_i\|_2 \\ &= \left\| X_{i+1} - X_i + k \sum_{l=1}^{n_{\text{stage}}} b_l (\mathbf{u}(X_{i+1}, t^j + c_l k) - \mathbf{u}(X_i, t^j + c_l k)) + O(k^2) \right\|_2 \\ & \quad - \|X_{i+1} - X_i\|_2 \\ &\leq [kL + O(k^2)] \|X_{i+1} - X_i\|_2 = O(kh_L), \end{aligned} \tag{6.23}$$

where the first equality follows from (6.13). Therefore we have

$$\begin{aligned} \Delta V_\varphi^j &= \sum_{i=0}^{N^j-1} \left(\left| \|p_{i+1} - p_i\|_2 - \frac{1}{3}h_L \right| - \left| \|X_{i+1} - X_i\|_2 - \frac{1}{3}h_L \right| \right) \\ &\leq \sum_{i=0}^{N^j-1} \left| \|p_{i+1} - p_i\|_2 - \frac{1}{3}h_L - \|X_{i+1} - X_i\|_2 + \frac{1}{3}h_L \right| \\ &= \sum_{i=0}^{N^j-1} O(kh_L) \\ &= O(k), \end{aligned}$$

where the first step follows from (6.20), the second from the triangle inequality, the third from (6.23), and the last from (6.22).

For (c), assume that we add p between p_i and p_{i+1} . Let X be the preimage of p at t_j . Note that p is the unique marker inserted to (p_i, p_{i+1}) for sufficiently small k and

$$\begin{aligned} \|p_{i+1} - p\|_2 &= \|X_{i+1} - X\|_2 + O(kh_L) \\ &= \frac{1}{2} \|X_{i+1} - X_i\|_2 + O(h_L^2) + O(kh_L), \end{aligned}$$

where the first equality follows from the same argument as (6.23), and the second from the adding marker scheme in (ARMS-2) and (4.28). Similarly,

$$\|p - p_i\|_2 = \frac{1}{2} \|X_{i+1} - X_i\|_2 + O(h_L^2) + O(kh_L).$$

Hence

$$\begin{aligned} \Delta V_\psi^{(1)} &= \left| \|p_{i+1} - p\|_2 - \frac{1}{3}h_L \right| + \left| \|p - p_i\|_2 - \frac{1}{3}h_L \right| - \left| \|p_{i+1} - p_i\|_2 - \frac{1}{3}h_L \right| \\ &= 2 \left| \frac{1}{2} \|X_{i+1} - X_i\|_2 + O(h_L^2) + O(kh_L) - \frac{1}{3}h_L \right| \\ & \quad - \left| \|X_{i+1} - X_i\|_2 + O(kh_L) - \frac{1}{3}h_L \right| \\ &= \|X_{i+1} - X_i\|_2 - \frac{2}{3}h_L - \left(\|X_{i+1} - X_i\|_2 - \frac{1}{3}h_L \right) + O(h_L^2) + O(kh_L) \\ &= -\frac{1}{3}h_L + O(h_L^2) + O(kh_L), \end{aligned}$$

where the second equality follows from (6.23), and the third from

$$\|X_{i+1} - X_i\|_2 = \|p_{i+1} - p_i\|_2 + O(kh_L) > h_L^* + O(kh_L) > \frac{2}{3}h_L$$

for sufficiently small k since (6.21), (6.23), and $\|p_{i+1} - p_i\| > h_L^*$.

For (d), we just consider removing one single marker in χ_{j+1} . Let p_i , p_{i+1} , and p_{i+2} satisfy $\|p_{i+1} - p_i\| = ah_L$ and $\|p_{i+2} - p_{i+1}\| = bh_L$ with $0 < a < r_{\text{tiny}}$ and $b > 0$. Then removing p_{i+1} results in

$$\begin{aligned} \Delta V_\chi^{(1)} &= \left| \|p_{i+2} - p_i\| - \frac{1}{3}h_L \right| - \left| \|p_{i+2} - p_{i+1}\| - \frac{1}{3}h_L \right| - \left| \|p_{i+1} - p_i\| - \frac{1}{3}h_L \right| \\ &= \left(\left| a + b + O(h_L) - \frac{1}{3} \right| - \left| b - \frac{1}{3} \right| - \left| a - \frac{1}{3} \right| \right) h_L \\ &= \begin{cases} \max(2(a+b) - 1 + O(h_L), -\frac{1}{3} + O(h_L)) h_L & \text{if } b \leq \frac{1}{3}; \\ (2a - \frac{1}{3} + O(h_L)) h_L & \text{if } b > \frac{1}{3} \end{cases} \\ &< 0, \end{aligned}$$

where the second equality holds because of the second-order accuracy of the line segment approximation when h_L is sufficiently small, and the last inequality follows from $a < r_{\text{tiny}} < \frac{1}{6}$. \square

Lemma 6.8. *If $r_{\text{tiny}} < \frac{1}{6}$, the total number of removed markers during the tracking is $O\left(\frac{1}{h_L}\right)$.*

Proof. Note that (b), (c), and (d) in Lemma 6.7 are the only ways to change the total variation V_j since the augmentation operation, the fully discrete mapping operation, and the adjustment operation completely consists of a MARS method as in (5.1). Denote the total number of adding markers by N_a and that of removing markers by N_r , then

$$\Delta V = V^n - V^0 = \sum_{j=0}^{n-1} \Delta V_\varphi^j + N_a \Delta V_\psi^{(1)} + N_r \Delta V_\chi^{(1)}, \quad (6.24)$$

which, together with Lemma 6.7, yields

$$\begin{aligned} \left| N_a \Delta V_\psi^{(1)} \right| &= -N_a \Delta V_\psi^{(1)} = -\Delta V + \sum_{j=0}^{n-1} \Delta V_\varphi^j + N_r \Delta V_\chi^{(1)} \\ &< -\Delta V + \sum_{j=0}^{n-1} \Delta V_\varphi^j = O(1) + O\left(\frac{1}{k}\right) \cdot O(k) = O(1). \end{aligned}$$

Combining with $\left| \Delta V_\psi^{(1)} \right| = \frac{1}{3}h_L + O(h_L^2) + O(kh_L)$ in Lemma 6.7(c), we obtain $N_a = O\left(\frac{1}{h_L}\right)$ and

$$N_r \leq N_a + N^0 = O\left(\frac{1}{h_L}\right),$$

which completes the proof. \square

By (6.18) and Lemma 6.8, the adjustment error accumulates as

$$E^{\text{ADJ}}(t_n) = \left\| \bigoplus_{j=1}^n \phi_{t_j}^{(n-j)k} [\varphi_{t_{j-1}}^k \mathcal{M}_\psi^{j-1}, \mathcal{M}^j] \right\| = O\left(\frac{1}{h_L}\right) \cdot O(h_L^5) = O(h_L^4). \quad (6.25)$$

The rest of this subsection is a proof of existence of the smooth curve $\partial \mathcal{M}_S^j$ mentioned at the beginning of this subsection.

A set of \mathcal{C}^∞ functions $\{\rho_\alpha : M \rightarrow [0, +\infty)\}_{\alpha \in I_\alpha}$ defined on a manifold M is called a \mathcal{C}^∞ *partition of unity* if $\sum_{\alpha \in I_\alpha} \rho_\alpha = 1$ and the corresponding set of supports, written $\{\text{supp } \rho_\alpha\}_{\alpha \in I_\alpha}$, is locally finite, i.e., any point $x \in M$ has a local neighborhood that meets only a finite number of supports in $\{\text{supp } \rho_\alpha\}_{\alpha \in I_\alpha}$.

Theorem 6.1 (Existence of a \mathcal{C}^∞ partition of unity). *For any open cover $\{U_\alpha\}_{\alpha \in I_\alpha}$ of a manifold M , there exists a \mathcal{C}^∞ partition of unity $\{\rho_\alpha\}_{\alpha \in I_\alpha}$ on M such that $\text{supp } \rho_\alpha \subset U_\alpha$ for every $\alpha \in I_\alpha$.*

Proof. See [22, Theorem 13.7]. \square

Lemma 6.9. *For any periodic or not-a-knot spline $\mathbf{p} : [l_0, l_N] \rightarrow \mathbb{R}^2$ with its cumulative chordal lengths as $(l_i)_{i=0}^N$, there exists a smooth curve $\gamma \in \mathcal{C}^\infty$ such that $\mathbf{p}(l_i) \in \gamma$ for each $i = 0, \dots, N$.*

Proof. For any positive real number $\epsilon < \frac{1}{4} \min_{i=1}^N |l_i - l_{i-1}|$, the 1-manifold $I_{\mathbf{p}} := (l_0 - \epsilon, l_N + \epsilon)$ has an open cover $(U_j)_{j=0}^{2N}$ given by

$$U_j := \begin{cases} \left(l_{\frac{j}{2}} - 2\epsilon, l_{\frac{j}{2}} + 2\epsilon \right) & \text{if } j \text{ is even;} \\ \left(l_{\frac{j-1}{2}} + \epsilon, l_{\frac{j-1}{2}+1} - \epsilon \right) & \text{if } j \text{ is odd.} \end{cases} \quad (6.26)$$

Theorem 6.1 implies the existence of a partition of unity $(\rho_j)_{j=0}^{2N}$ satisfying $\text{supp } \rho_j \subset U_j$ and $\sum_{j=0}^{2N} \rho_j \equiv 1$ on $I_{\mathbf{p}}$, which, together with (6.26), further yield

$$\begin{cases} \forall i = 0, \dots, N, \quad \forall l \in (l_i - \epsilon, l_i + \epsilon), \quad \rho_{2i}(l) = 1; \\ \forall i = 0, \dots, N-1, \quad \forall l \in (l_i + 2\epsilon, l_{i+1} - 2\epsilon), \quad \rho_{2i+1}(l) = 1. \end{cases}$$

For each $i = 0, \dots, N-1$, we construct $\mathbf{q}_i \in \mathbb{P}_2 \times \mathbb{P}_2$ over $(l_i - 2\epsilon, l_i + 2\epsilon)$ by requiring $\mathbf{q}_i(l_i) = \mathbf{p}(l_i)$ and $\frac{d^2 \mathbf{q}_i}{ds^2}(l_i) = \frac{d^2 \mathbf{p}}{ds^2}(l_i)$. For a periodic spline, we also set $\mathbf{q}_N(l) := \mathbf{q}_1(l - l_N)$.

Now we define a curve $\gamma : I_{\mathbf{p}} \rightarrow \mathbb{R}^2$ by

$$\gamma(l) := \sum_{i=0}^N \rho_{2i}(l) \mathbf{q}_i(l) + \sum_{i=0}^{N-1} \rho_{2i+1}(l) \mathbf{p}_i(l) \quad (6.27)$$

where $\mathbf{p}_i := \mathbf{p}|_{(l_i, l_{i+1})}$ is the pair of polynomials of \mathbf{p} on the i th interval. By the above construction, γ is in \mathcal{C}^∞ . In particular, a periodic spline satisfies

$$\gamma^{(j)}(l_N) = [\rho_{2N}(l_N) \mathbf{q}_N(l_N)]^{(j)} = \mathbf{q}_N^{(j)}(l_N) = \mathbf{q}_0^{(j)}(0) = [\rho_0(l_0) \mathbf{q}_0(l_0)]^{(j)} = \gamma^{(j)}(l_0)$$

for any nonnegative integer j . \square

6.6. Summary

The main result of this section is

Theorem 6.10. *For $r_{\text{tiny}} < \frac{1}{6}$, the IT error of the multiphase MARS method in Definition 5.7 for tracking each of the multiple phases is*

$$\forall T > t_0, \quad E_{\text{IT}}(T) = O(h_L^4) + O(k^\kappa), \quad (6.28)$$

where κ denotes the order of the ODE solver and h_L is the maximum chordal length in the (r_{tiny}, h_L) -regularity satisfied by each marker sequence.

Proof. This follows from Theorem 6.2, (6.10), (6.11), Lemma 6.5 and (6.25). \square

On top of Theorem 6.10, the convergence of the multiphase MARS method follows from the stability of the employed time integrator.

7. Tests

In this section, we perform a number of classical benchmark tests to demonstrate the high accuracy of the proposed MARS method in tracking multiple materials. For fourth-, sixth-, and eighth-order approximations of the exact flow map, we use the classic fourth-order Runge–Kutta method, the explicit one-step method by Verner,²³ and that by Dormand and Prince,¹⁰ respectively. These methods are chosen solely based on ease of implementation, and the convergence rates of the MARS method would be qualitatively the same if another explicit time integrator of the same order were employed.

By (6.6), the IT error of a phase \mathcal{M}_i at time t_n is given by

$$E_i^g(t_n) = \|\mathcal{M}_i(t_n) \oplus \mathcal{M}_i^n\| = \sum_{\mathcal{C}_j \subset \Omega} \|(\mathcal{M}_i(t_n) \cap \mathcal{C}_j) \oplus (\mathcal{M}_i^n \cap \mathcal{C}_j)\|, \quad (7.1)$$

where \mathcal{M}_i^n is the computed result that follows from $\tilde{\Gamma}^n$ and approximates the exact result $\mathcal{M}_i(t_n)$ while \mathcal{C}_j 's are the control volumes that partition the computational domain Ω , i.e., $\bigcup_j^{\perp\perp} \mathcal{C}_j = \Omega$ and $\mathbf{i} \neq \mathbf{j} \implies \mathcal{C}_i \cap \mathcal{C}_j = \emptyset$.

As $h \rightarrow 0$, the computation of symmetric differences in (7.1) tends to be more and more ill-conditioned. Hence in practice we approximate E_i^g with

$$E_i(t_n) := \sum_{\mathcal{C}_j \subset \Omega} \left| \|\mathcal{M}_i(t_n) \cap \mathcal{C}_j\| - \|\mathcal{M}_i^n \cap \mathcal{C}_j\| \right|. \quad (7.2)$$

We also define the *total IT error* as $\sum_{i=1}^{N_p} E_i$.

Table 1. IT Errors and convergence rates of the proposed cubic MARS method for solving the vortex shear test of $T = 4, 8, 12, 16$. The first part is based on $\sum_{i=1}^5 E_i$ while the second on E_i in (7.2). The time step size is $k = \frac{1}{8}h$ for the constant and curvature-based ARMS, respectively.

Results based on $\sum_{i=1}^5 E_i$		$h = \frac{1}{32}$	rate	$h = \frac{1}{64}$	rate	$h = \frac{1}{128}$
$T = 4$, constant ARMS with $r_{\text{tiny}} = 0.05$	$h_L = 0.2h$	2.73e-09	3.95	1.77e-10	4.02	1.09e-11
	$h_L = 1.5h^{\frac{3}{2}}$	9.03e-09	6.06	1.35e-10	5.98	2.15e-12
	$h_L = 10h^2$	1.88e-08	8.18	6.50e-11	7.79	2.93e-13
$T = 8$, constant ARMS with $r_{\text{tiny}} = 0.01$	$h_L = 0.2h$	8.67e-09	4.16	4.86e-10	3.96	3.12e-11
	$h_L = 1.5h^{\frac{3}{2}}$	3.89e-08	6.71	3.71e-10	5.95	6.02e-12
	$h_L = 10h^2$	7.57e-08	8.74	1.77e-10	7.91	7.38e-13
$T = 12$, curvature-based ARMS with (7.4) & $r_{\min}^c = 0.01$	$h_L^c = 0.2h$	2.37e-09	3.82	1.68e-10	3.96	1.08e-11
	$h_L^c = 1.5h^{\frac{3}{2}}$	6.81e-09	5.85	1.18e-10	6.15	1.66e-12
	$h_L^c = 10h^2$	1.44e-08	8.18	4.95e-11	7.54	2.67e-13
$T = 16$, curvature-based ARMS with (7.4) & $r_{\min}^c = 0.005$	$h_L^c = 0.2h$	3.18e-09	3.84	2.22e-10	4.04	1.35e-11
	$h_L^c = 1.5h^{\frac{3}{2}}$	1.46e-08	6.45	1.67e-10	6.13	2.38e-12
	$h_L^c = 10h^2$	1.74e-08	7.91	7.25e-11	7.73	3.41e-13
Results based on E_i		$h = \frac{1}{32}$	rate	$h = \frac{1}{64}$	rate	$h = \frac{1}{128}$
$T = 16$, curvature-based ARMS with $h_L^c = 0.2h$, (7.4), and $r_{\min}^c = 0.005$	phase					
	blue	6.87e-10	3.72	5.21e-11	4.08	3.08e-12
	cyan	7.07e-10	3.84	4.92e-11	4.11	2.86e-12
	red	4.53e-10	3.93	2.96e-11	4.01	1.83e-12
	green	5.37e-10	3.84	3.74e-11	4.07	2.22e-12
	white	7.97e-10	3.90	5.35e-11	3.93	3.51e-12

7.1. Vortex shear of a quartered circular disk

Referring to Definition 3.2, the flow map of this test is that of the ODE $\frac{d\mathbf{X}}{dt} = \mathbf{u}(\mathbf{X}, t)$ with $\mathbf{u} = (\frac{\partial\psi}{\partial y}, -\frac{\partial\psi}{\partial x})$ determined from the stream function

$$\psi(x, y) = -\frac{1}{\pi} \sin^2(\pi x) \sin^2(\pi y) \cos\left(\frac{\pi t}{T}\right), \quad (7.3)$$

where the time period $T = 4, 8, 12, 16$. At time $t = \frac{T}{2}$, the velocity field is reversed by the cosinusoidal temporal factor so that the exact solution $(\mathcal{M}_i(t))_{i=1}^5$ at $t = T$ is the same as the initial condition $(\mathcal{M}_i(t_0))_{i=1}^5$ at $t_0 = 0$. As shown in Fig. 6(a), the four colored Yin sets constitute a circular disk with its radius as 0.15 and its center at $[0.5, 0.75]^T$ while the last Yin set is the unbounded complement of the circle.

For this IT problem of five phases, the cases $T = 4, 8$ are solved by the proposed MARS method of the constant ARMS strategy while the cases $T = 12, 16$ by that of the curvature-based ARMS strategy (5.10) with

$$r_{\text{tiny}} = 0.1; (\rho_{\min}^c, \rho_{\max}^c) = (10^{-5}, 0.2); r_{\min}^c = 0.01, 0.005; \sigma^c(x) = x. \quad (7.4)$$

The time step sizes are set to $k = \frac{1}{8}h$ for $T = 4, 8, 12, 16$, so that IT errors are dominated not by temporal discretizations of flow maps but by spatial approximations of the interface; otherwise the temporal symmetry in (7.3) would

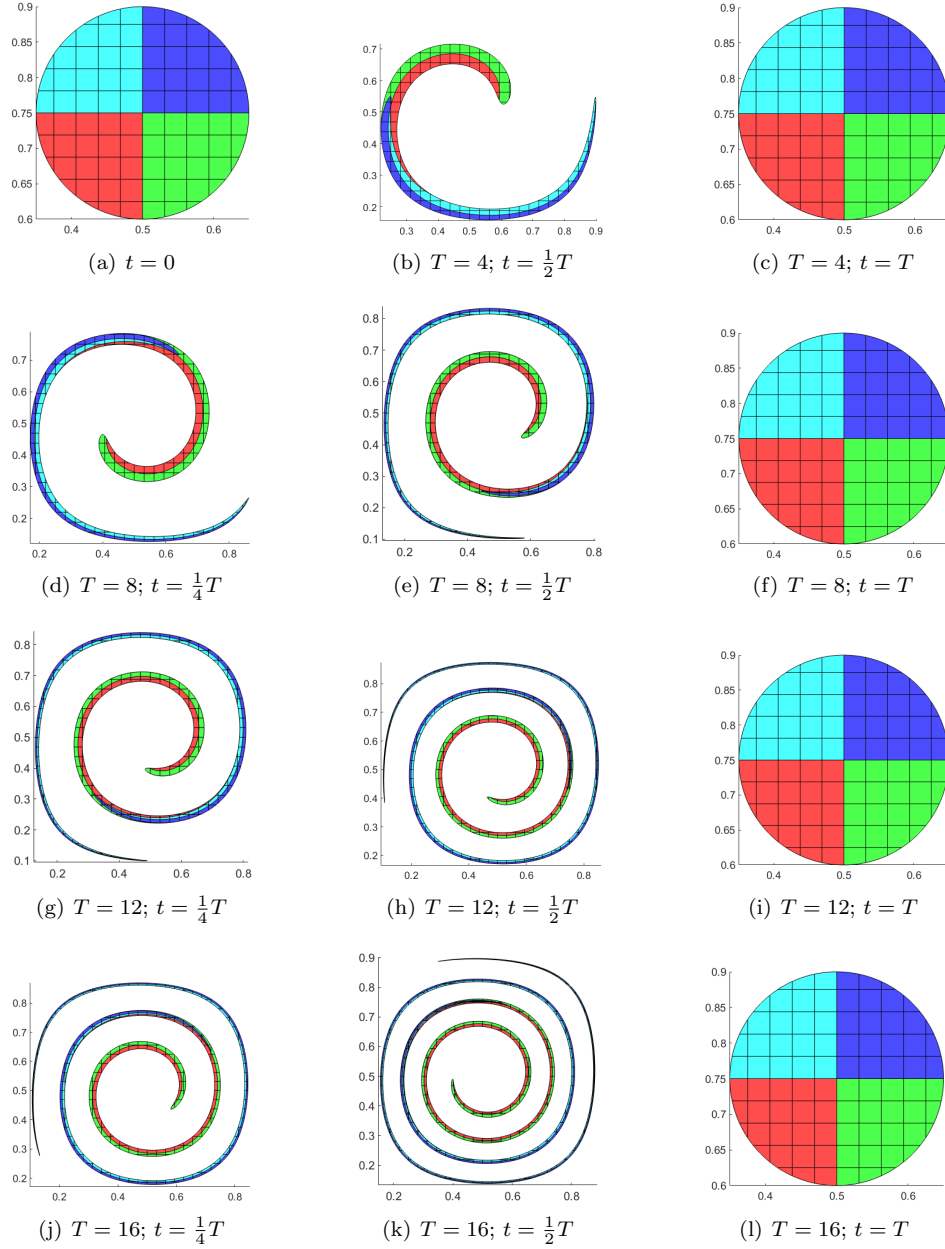


Fig. 6. Solutions of the cubic MARS method for the vortex shear test with $T = 4, 8, 12, 16$ on the Eulerian grid of $h = \frac{1}{32}$. The initial distances between adjacent markers for $T = 4, 8$ and $T = 12, 16$ are respectively set to the uniform constant $0.1h$ and the varying value $\frac{1}{2}h_L(\rho)$ with h_L defined in (5.10). See Table 1 for values of other parameters.

Table 2. Total IT errors $\sum_i E_i$ and convergence rates of cubic MARS methods compared with those of VOF/MOF methods in solving three vortex-shear tests. For test (a), the last three lines are taken from [20, Tab. 7], where the two-letter acronyms LV, NI, MC, and MB stand for the LVIRA algorithm,¹⁷ de Niem’s intersection check method,⁸ Mosso and Clancy’s method,¹⁶ and a combination of MC¹⁶ and Benson’s method,³ respectively. The last two lines for tests (b) and (c) are taken from [12, Tab. 2] and [12, Tab. 4], respectively. For all MARS methods, we use $h_L = 0.2h$ or $h_L^c = 0.2h$; see Table 1 for values of other parameters.

(a): the three-phase vortex-shear test in [20, Sec. 3.5] with $T = 8$					
method	$h = \frac{1}{32}$	rate	$h = \frac{1}{64}$	rate	$h = \frac{1}{128}$
constant ARMS	3.56e-09	3.97	2.28e-10	3.98	1.45e-11
LV + NI	3.21e-02	1.16	1.44e-02	1.22	6.16e-03
LV + MC	2.91e-02	1.17	1.29e-02	1.10	6.02e-03
LV + MB	2.28e-02	1.05	1.11e-02	0.89	5.95e-03
(b): the two-phase vortex-shear test in [12, Sec. 4.3] with $T = 8$					
method	$h = \frac{1}{32}$	rate	$h = \frac{1}{64}$	rate	$h = \frac{1}{128}$
constant ARMS	4.73e-09	3.87	3.23e-10	3.91	2.14e-11
Standard MOF	1.42e-02	0.92	7.46e-03	2.53	1.29e-03
MOF by Jemison ¹⁴	3.12e-03	2.17	6.91e-04	1.31	2.77e-04
(c): the two-phase vortex-shear test in [12, Sec. 4.4] with $T = 12$					
method	$h = \frac{1}{32}$	rate	$h = \frac{1}{64}$	rate	$h = \frac{1}{128}$
curvature-based ARMS	1.72e-09	3.87	1.18e-10	4.01	7.33e-12
standard MOF for two phases	2.66e-02	0.55	1.81e-02	2.42	3.37e-03
MOF by Hergibo et al. ¹²	4.98e-03	2.32	9.91e-04	1.99	2.48e-04

lead to convergence rates higher than expected, such as those in Table 4. In (7.4), we use $r_{\text{tiny}} = 0.1$ to limit to one order of magnitude the difference of chordal lengths caused by the *random* tangential advection of markers. The values $(\rho_{\min}^c, \rho_{\max}^c) = (10^{-5}, 0.2)$ come from the presence of line segments in the initial condition and the fact of the radius of the initial circle being 0.15. As T increases from 12 to 16, we decrease r_{\min}^c from 0.01 to 0.005 to account for the larger deformation.

In Fig. 6, we plot our solutions on the Eulerian grid of $h = \frac{1}{32}$ at key time instances. During the entire simulation, the interface graph $G_\Gamma = (V_\Gamma, E_\Gamma, \psi_\Gamma)$ that represents the initial topology of the five phases remains the same: E_Γ always consists of the eight edges that connect the five vertices in $V_\Gamma = J_\Gamma$, i.e., the four T junctions on the circle and the X junction inside the circle. By Algorithm 1, C_S contains only a single circuit of the four T junctions while T_S has two trails that correspond to the two disk diameters. The constancy of these topological data confirms the validity and efficiency of separating topology from geometry. On the other hand, the spline curves corresponding to circuits in C_S and trails in T_S are reconstructed at each time step. Despite the enormous deformations and the large size of the Eulerian grid, each phase remains connected without generating any

flotsam and the difference between the final solution and the initial condition is indiscernible.

To visually compare results of MARS and VOF methods reviewed in Sec. 1, we note that the vortex shear test with $T = 4$ is the same as that in [19, Sec. 5.5]. Thus Fig. 6(a,b,c) compares directly to [19, Fig. 17], where both the material-order-dependent Young's method²⁴ and the material-order-independent power diagram method¹⁹ generate flotsam, failing to preserve the connectedness of the deforming phases. Also shown in [19, Fig. 17] are the prominently different geometric features between the final solutions and the initial conditions of these VOF methods.

In Table 1 we present, for all cases of $T = 4, 8, 12, 16$, total IT errors $\sum_{i=1}^5 E_i$ and convergence rates of MARS methods with both constant and curvature-based ARMS strategies. For $T = 16$ and $h_L^c = 0.2h$, we also show, for each individual phase, results based on E_i in (7.2). In all cases and for all phases, fourth-, sixth-, and eighth-order convergence rates are clearly demonstrated for the choices of h_L or h_L^c being $O(h)$, $O(h^{\frac{3}{2}})$, and $O(h^2)$, respectively. The smallest total errors 2.93×10^{-13} and 2.67×10^{-13} indicate excellent conditioning of both ARMS strategies.

To quantitatively compare MARS with VOF/MOF methods, we first quote from [19, p. 744] that, for the test of $T = 4$ with $h = \frac{1}{64}$ and $k = \frac{1}{8}h$, the smallest IT errors of Young's method²⁴ and the power diagram method¹⁹ are respectively 1.28×10^{-3} and 1.35×10^{-4} , which are much larger than 2.73×10^{-9} , the total IT error of MARS in the case of $h = \frac{1}{32}$, $h_L = 0.2h$, and $k = \frac{1}{8}h$ in Table 1. Then in Table 2 we compare our cubic MARS method with VOF/MOF methods for solving three other vortex-shear tests in the literature. The circular disk in test (a) consists of three phases with two triple points while tests (b) and (c) are the classic two-phase test with $T = 8$ and 12, respectively. For all tests, the proposed cubic MARS method is more accurate than VOF/MOF methods by many orders of magnitude.

7.2. Deformation of a circular disk divided into five phases

The flow map of this test is determined by the same mechanism as that in Sec. 7.1, with the stream function as

$$\psi(x, y) = -\frac{1}{n_v \pi} \sin(n_v \pi(x + 0.5)) \cos(n_v \pi(y + 0.5)) \cos\left(\frac{\pi t}{T}\right), \quad (7.5)$$

where $T = 2, 4$ and the number of vortices is $n_v = 4$. At $t = \frac{T}{2}$, the temporal factor reverses the velocity field so that the exact solution $(\mathcal{M}_i(t))_{i=1}^6$ at $t = T$ is identical to the initial condition $(\mathcal{M}_i(t_0))_{i=1}^6$ at $t_0 = 0$. As shown in Fig. 7 (a), the five colored Yin sets constitute a circular disk with its radius as $r = 0.15$ and its center at $[0.5, 0.5]^T$ while the last Yin set is the unbounded complement of the circle.

The above IT problem of six phases is numerically solved by the cubic MARS method with the curvature-based ARMS strategy (5.10) specified by

$$r_{\text{tiny}} = 0.05; (\rho_{\min}^c, \rho_{\max}^c) = (10^{-5}, 1); r_{\min}^c = 0.1, 0.05; \sigma^c(x) = x. \quad (7.6)$$

Different from those in (7.4), the parameter values in (7.6) are suitable for the deformation tests. For example, the higher value of ρ_{\max}^c accounts for the much

Table 3. Errors and convergence rates of the cubic MARS method of curvature-based ARMS with $k = \frac{1}{8}h$ for solving the deformation test of $T = 2, 4$.

Results based on $\sum_{i=1}^6 E_i$	h_L^c	$h = \frac{1}{32}$	rate	$h = \frac{1}{64}$	rate	$h = \frac{1}{128}$
$T = 2$, curvature-based ARMS with (7.6) and $r_{\min}^c = 0.1$	$0.2h$	5.53e-09	3.97	3.54e-10	4.03	2.16e-11
	$1.5h^{\frac{3}{2}}$	1.74e-08	5.99	2.74e-10	5.98	4.33e-12
	$10h^2$	3.24e-08	8.00	1.27e-10	7.95	5.14e-13
$T = 4$, curvature-based ARMS with (7.6) and $r_{\min}^c = 0.05$	$0.2h$	7.10e-09	4.10	4.15e-10	4.10	2.43e-11
	$1.5h^{\frac{3}{2}}$	1.79e-08	5.77	3.28e-10	6.04	4.98e-12
	$10h^2$	3.36e-08	7.85	1.46e-10	8.17	5.07e-13
Results based on E_i	phase	$h = \frac{1}{32}$	rate	$h = \frac{1}{64}$	rate	$h = \frac{1}{128}$
$T = 4$, curvature-based ARMS with $h_L^c = 0.2h$, (7.6), and $r_{\min}^c = 0.05$	blue	9.59e-10	4.15	5.41e-11	4.18	2.98e-12
	red	7.19e-10	4.37	3.47e-11	4.17	1.93e-12
	green	1.37e-09	3.87	9.32e-11	3.97	5.95e-12
	white	2.44e-09	4.06	1.47e-10	4.09	8.58e-12

larger percentage of low-curvature arcs in Fig. 7 than that in Fig. 6. As T increases from 2 to 4, we decrease r_{\min}^c from 0.1 to 0.05 to account for the larger deformations. For $T = 2, 4$, the maximum density-increase ratios, as well as the maximum ratios of the longest chordal length over the shortest one, are respectively $R_{\max} = 200, 400$, which ensures good conditioning of spline fitting.

As shown in Fig. 7, the interface graph $G_\Gamma = (V_\Gamma, E_\Gamma, \psi_\Gamma)$ that represents the interface topology remains the same during the entire simulation: E_Γ always consists of the ten edges that connect the five T junctions located on the circle and the junction of degree 5 at the disk center. By Algorithm 1, C_S contains a single circuit formed by the five T junctions while T_S has five trails that correspond to the five disk radii. Despite the tremendous deformations, each phase remains connected, demonstrating the capability of our method in preserving topological structures.

As shown in Fig. 7(g,i), the boundary lengths increase and decrease. Accordingly, in Fig. 7(h,j), the number of interface markers for each phase first increases, then stagnates roughly as a constant, and finally decreases. For the number of markers, the increase and decrease are clearly driven by those of the boundary length while the stagnation follows from the finite width of the interval $[r_{\text{tiny}}h_L, h_L]$ and the fact that it takes time for the distances of adjacent markers to decrease from h_L to $r_{\text{tiny}}h_L$. At the end of the simulation, the number of markers for each phase is roughly twice as much as that at the initial time. This ratio being around 2, together with the similarity between subplots (g,i) and (h,j) in Fig. 7, illustrates the versatility and effectiveness of ARMS in managing the regularity of interface markers.

The IT errors and convergence rates of the proposed MARS method are listed in

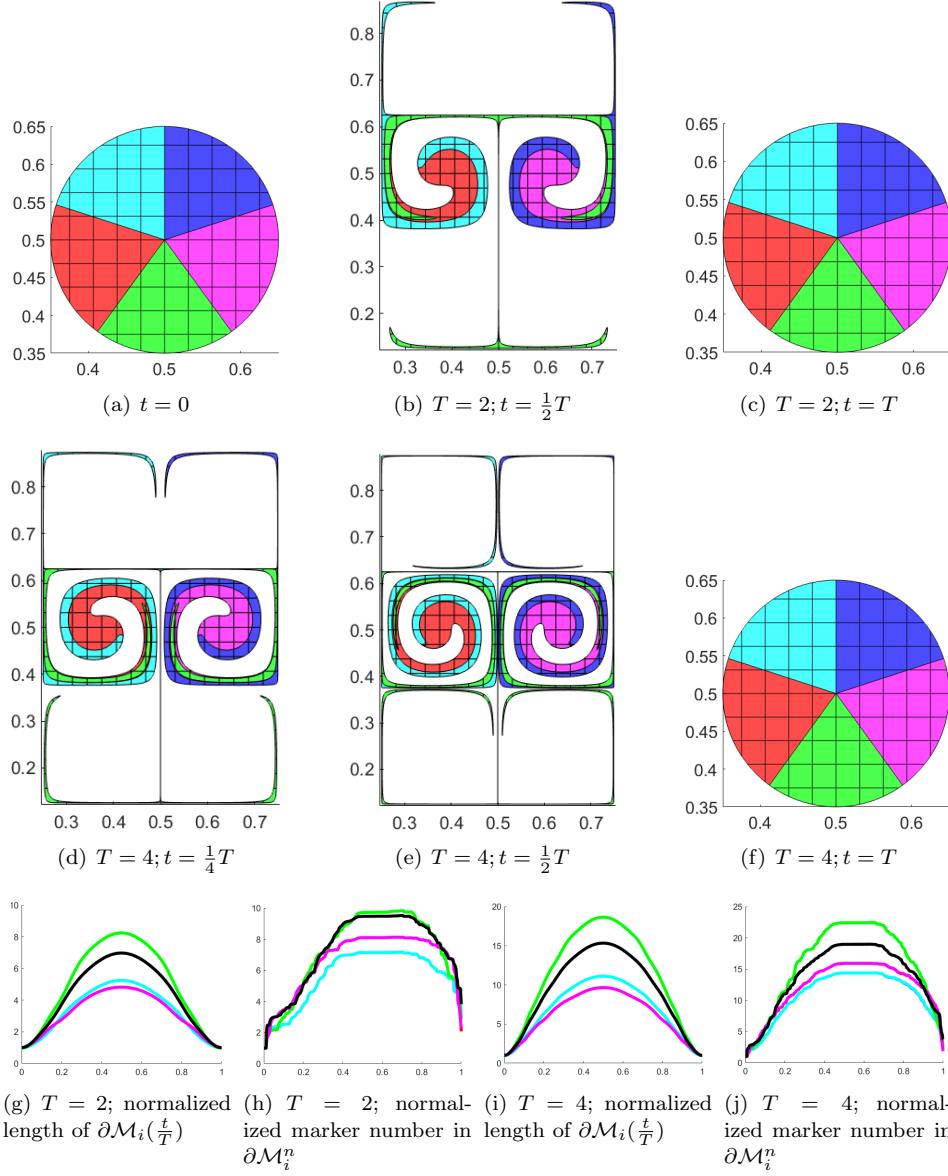


Fig. 7. Solutions of the cubic MARS method with $h_L^c = 0.2h$ for the deformation test of $T = 2$ and $T = 4$ on the Eulerian grid of $h = \frac{1}{32}$. Subplots (a)–(f) are snapshots of the solution at key time instants. In subplots (g)–(j), each phase is represented by a curve of the same color except that the white phase (the unbounded complement of the circle) is represented by the black curve. Due to symmetry, the red and blue curves may not be visible. The initial distances between markers are $\frac{1}{2}h_L(\rho)$, where h_L is defined in (5.10). See Table 3 for values of other parameters.

Table 4. IT errors and convergence rates based on (7.2) of some representative phases in solving the deformation test of $T = 2$ by the cubic MARS method with different ARMS strategies. The second tabular contains errors at $t = \frac{1}{2}T$ by Richardson extrapolation.

method	phase	$h = \frac{1}{32}$	rate	$h = \frac{1}{64}$	rate	$h = \frac{1}{128}$
constant ARMS with $k = \frac{1}{8}h$ and (r_{tiny}, h_L) = (0.005, 0.2h)	blue	5.67e-08	4.19	3.11e-09	5.36	7.60e-11
	red	1.07e-08	3.94	6.99e-10	3.70	5.38e-11
	green	1.85e-08	3.94	1.20e-09	3.98	7.60e-11
	white	1.21e-07	4.21	6.55e-09	5.23	1.74e-10
curvature-based ARMS with $k = \frac{1}{8}h$, $h_L^c = 0.2h$, (7.6), and $r_{\min}^c = 0.1$.	blue	7.22e-10	3.93	4.74e-11	4.19	2.59e-12
	red	5.22e-10	4.13	2.99e-11	3.95	1.93e-12
	green	1.19e-09	3.85	8.25e-11	3.85	5.72e-12
	white	1.89e-09	3.98	1.20e-10	4.07	7.14e-12
curvature-based ARMS with $k = h$, $h_L^c = 0.2h$, (7.6), and $r_{\min}^c = 0.1$.	blue	3.20e-06	4.84	1.12e-07	5.00	3.51e-09
	red	4.23e-06	4.98	1.34e-07	4.99	4.24e-09
	green	2.98e-06	4.96	9.57e-08	5.00	3.00e-09
	white	6.97e-06	4.97	2.22e-07	5.00	6.96e-09
$t = \frac{1}{2}T$	phase	$\frac{1}{16} - \frac{1}{32}$	rate	$\frac{1}{32} - \frac{1}{64}$	rate	$\frac{1}{64} - \frac{1}{128}$
curvature-based ARMS with $k = \frac{1}{8}h$, $h_L^c = 0.2h$, (7.6), and $r_{\min}^c = 0.1$.	blue	1.51e-08	3.56	1.28e-09	3.98	8.10e-11
	red	1.64e-08	3.98	1.04e-09	3.79	7.52e-11
	green	2.71e-08	4.05	1.63e-09	3.97	1.04e-10
	white	5.09e-08	3.82	3.60e-09	4.12	2.08e-10

Table 5. Accuracy comparison of the cubic MARS method ($h_L^c = 0.2h$; $k = \frac{1}{8}h$) with some VOF methods based on the total IT error $\sum_{i=1}^3 E_i$ for the three-phase deformation test in [20, Sec. 3.6]. The curvature-based ARMS is specified by (7.6) and $r_{\min}^c = 0.1$. The errors in the last three lines are taken from [20, Tab. 8], with the two-letter acronyms defined in the caption of Table 2.

method	$h = \frac{1}{32}$	rate	$h = \frac{1}{64}$	rate	$h = \frac{1}{128}$
curvature-based ARMS	3.69e-09	3.98	2.34e-10	4.14	1.33e-11
LV + NI	3.05e-02	0.92	1.61e-02	1.39	6.13e-03
LV + MC	2.37e-02	0.80	1.37e-02	1.16	6.10e-03
LV + MB	2.10e-02	0.76	1.25e-02	1.05	6.00e-03

Table 3, where convergence rates are close to 4, 6, and 8 for the choices of h_L^c being $O(h)$, $O(h^{\frac{3}{2}})$, and $O(h^2)$, respectively. In Table 4, we compare results of different ARMS strategies. Convergence rates of constant ARMS vary from one phase to another, indicating that, even with $r_{\text{tiny}} = 0.005$, the computation has not yet reached the asymptotic range. In contrast, convergence rates of curvature-based ARMS are more phase-independent, implying more efficient marker distributions that have

well resolved the high-curvature arcs. Finally, an increase of the time step size from $k = \frac{1}{8}h$ to $k = h$ yields convergence rates very close to five, implying the dominance of temporal discretization errors over the spatial approximation errors. The last tabular in Table 4 contains errors of phases at $t = \frac{1}{2}T$ by Richardson extrapolation, also indicate that our method converge rate is independent of periodicity of the velocity field.

Finally, results of MARS and some VOF methods for solving another deformation test in [20, Sec. 3.6] are compared in Table 5, which shows that the proposed MARS method is more accurate than these VOF methods by many orders of magnitude.

7.3. Vortex shear and deformation of the six phases in Fig. 2(a)

The flow maps of this test are the same as those in (7.3) and (7.5). Initial conditions of the tracked phases are the five Yin sets $(\mathcal{M}_i)_{i=1}^5$ shown in Fig. 2(a), whose boundaries are approximated to sufficient accuracy by \mathcal{C}^4 quintic splines, elliptical arcs, rose curves, and linear segments.

Parameters of the curvature-based ARMS strategy for the flow map of vortex shear are

$$r_{\text{tiny}} = 0.1; \quad (\rho_{\min}^c, \rho_{\max}^c) = (10^{-5}, 0.2); \quad \sigma^c(x) = x \quad (7.7)$$

while those for the flow map of deformation are

$$r_{\text{tiny}} = 0.05; \quad (\rho_{\min}^c, \rho_{\max}^c) = (10^{-5}, 1); \quad \sigma^c(x) = x, \quad (7.8)$$

where the parameter ρ_{\max}^c is selected based on the characteristics of flow fields. As for ρ_{\min}^c , we choose it as a monotonically decreasing function of the period T ; see Table 6 for its value of each test case.

As shown in Fig. 8, the interface graph that represents the interface topology remains the same during the entire simulation for both the vortex shear test and the deformation test: C_S always contains three circuits and T_S always has four trails. Despite the extremely large deformations, each phase remains connected. These invariants demonstrate the capability of the multiphase cubic MARS method in preserving topological structures.

The evolution of the boundary length and number of markers for each test and each phase is shown in Fig. 8 (g)–(j), demonstrating the effectiveness and versatility of ARMS in maintaining the (r, h) -regularity even for geometrically and topologically complex interfaces with high curvature ($r_{\min}^c \leq 0.01$).

Finally, we list, for this test, the IT errors and convergence rates in Table 6, which clearly show the fourth-, sixth-, and eighth- convergence rates for $h_L^c = O(h)$, $O(h^{3/2})$, and $O(h^2)$, respectively.

8. Conclusion

We have developed a cubic MARS method with a curvature-based ARMS strategy for fourth- and higher-order IT of multiple materials. The geometry of the interface

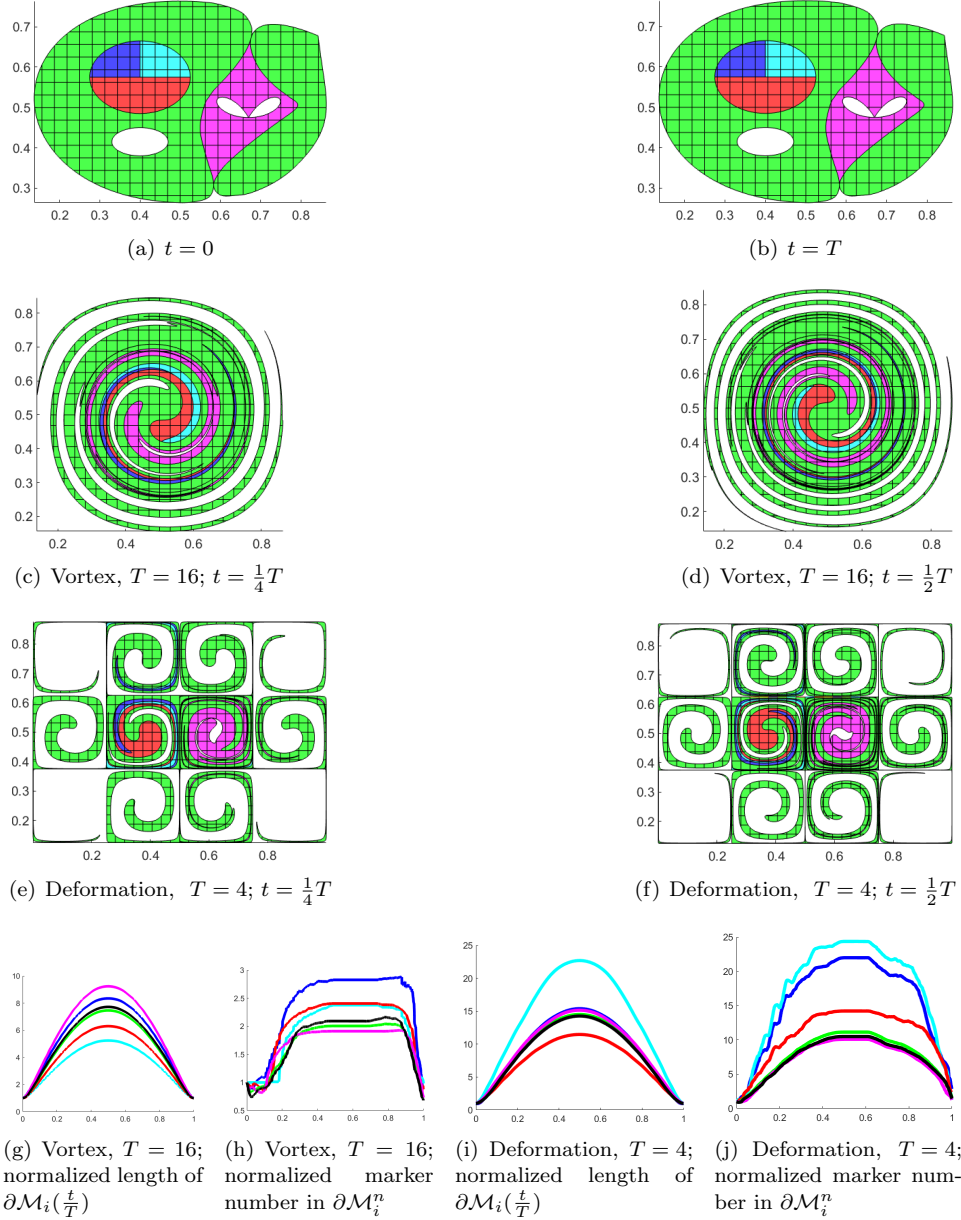
52 *Y. Tan & Y. Qian & Z. Li & Q. Zhang*


Fig. 8. Solutions of the cubic MARS method with $h_L^c = 0.2h$ for the vortex shear test ($T = 16$) and the deformation test ($T = 4$) on the Eulerian grid of $h = \frac{1}{32}$. Subplot (a) shows the initial Yin sets, which are the same as those in Fig. 2(a), and subplot (b) presents the final solutions of the two tests, which are visually indistinguishable. Subplots (c)–(f) are solution snapshots at key time instances. In subplots (g)–(j), each phase is represented by a curve of the same color except that the unbounded white phase is represented by the black curve. The initial distances between markers are $\frac{1}{2}h_L(\rho)$, where h_L is defined in (5.10).

Table 6. Errors and convergence rates of the cubic MARS method with curvature-based ARMS (using $k = \frac{1}{8}h$) for the vortex shear test at $T = 4, 8, 12, 16$ and the deformation test at $T = 2, 4$. The initial Yin sets are shown in Fig. 8(a).

Results based on $\sum_{i=1}^6 E_i$	h_L^c	$h = \frac{1}{32}$	rate	$h = \frac{1}{64}$	rate	$h = \frac{1}{128}$
Vortex, $T = 4$, curvature-based ARMS with (7.7) & $r_{\min}^c = 0.02$	$0.2h$	3.99e-10	3.78	2.91e-11	4.05	1.76e-12
	$1.5h^{\frac{3}{2}}$	1.50e-09	6.14	2.12e-11	5.86	3.66e-13
	$10h^2$	2.11e-09	7.58	1.10e-11	7.11	8.01e-14
Vortex, $T = 8$, curvature-based ARMS with (7.7) & $r_{\min}^c = 0.02$	$0.2h$	2.24e-09	3.87	1.53e-10	3.93	1.00e-11
	$1.5h^{\frac{3}{2}}$	7.10e-09	5.91	1.18e-10	5.94	1.92e-12
	$10h^2$	1.71e-08	8.10	6.20e-11	7.68	3.03e-13
Vortex, $T = 12$, curvature-based ARMS with (7.7) & $r_{\min}^c = 0.01$	$0.2h$	5.77e-09	4.07	3.43e-10	4.16	1.91e-11
	$1.5h^{\frac{3}{2}}$	1.41e-08	5.96	2.26e-10	5.90	3.78e-12
	$10h^2$	3.83e-08	8.45	1.10e-10	7.65	5.47e-13
Vortex, $T = 16$, curvature-based ARMS with (7.7) & $r_{\min}^c = 0.005$	$0.2h$	7.37e-09	4.14	4.19e-10	4.06	2.52e-11
	$1.5h^{\frac{3}{2}}$	2.01e-08	6.11	2.91e-10	5.86	5.02e-12
	$10h^2$	2.78e-08	8.03	1.06e-10	7.55	5.66e-13
Deformation, $T = 2$, curvature-based ARMS with (7.8) & $r_{\min}^c = 0.1$	$0.2h$	1.57e-08	3.84	1.09e-09	3.98	6.92e-11
	$1.5h^{\frac{3}{2}}$	5.05e-08	5.90	8.44e-10	6.00	1.31e-11
	$10h^2$	1.02e-07	8.00	3.99e-10	7.98	1.59e-12
Deformation, $T = 4$, curvature-based ARMS with (7.8) & $r_{\min}^c = 0.01$	$0.2h$	1.74e-08	3.95	1.13e-09	4.13	6.44e-11
	$1.5h^{\frac{3}{2}}$	5.02e-08	6.02	7.72e-10	5.97	1.23e-11
	$10h^2$	1.02e-07	8.02	3.94e-10	7.93	1.62e-12
Results based on E_i	phase	$h = \frac{1}{32}$	rate	$h = \frac{1}{64}$	rate	$h = \frac{1}{128}$
Vortex, $T = 16$, curvature-based ARMS with $h_L^c = 0.2h$, (7.7), and $r_{\min}^c = 0.005$	blue	4.71e-10	4.01	2.92e-11	4.03	1.79e-12
	cyan	3.40e-10	4.25	1.78e-11	4.00	1.11e-12
	red	2.53e-10	4.11	1.47e-11	3.48	1.32e-12
	green	3.24e-09	4.15	1.83e-10	4.06	1.09e-11
	pink	1.66e-09	4.45	7.60e-11	4.21	4.11e-12
	white	1.40e-09	3.83	9.84e-11	4.05	5.92e-12
Deformation, $T = 4$, curvature-based ARMS with $h_L^c = 0.2h$, (7.8), and $r_{\min}^c = 0.01$	blue	8.75e-10	4.07	5.20e-11	3.98	3.29e-12
	cyan	1.06e-09	4.07	6.31e-11	3.93	4.13e-12
	red	9.81e-10	4.00	6.13e-11	4.30	3.11e-12
	green	7.77e-09	3.96	4.99e-10	4.16	2.80e-11
	pink	2.58e-09	3.82	1.83e-10	4.10	1.07e-11
	white	4.14e-09	3.93	2.71e-10	4.16	1.52e-11

is approximated by cubic splines while the topology of these phases is represented by an undirected graph and a cycle set. For homeomorphic flow maps, the separation of the topology from the geometry leads to simple, efficient, and accurate algorithms in that topological structures are determined from the initial condition once and for all while evolving the interface only entails advancing the periodic and not-a-knot

cubic splines. The superior efficiency and accuracy of our method are demonstrated by results of several classic benchmark tests.

Several future research prospects follow. First, the Yin space, the MARS framework, and this work form a solid foundation to tackle topological changes of multiple phases. We will develop theoretical characterizations and design highly accurate algorithms for these topological changes. Second, we will couple this work with the PLG algorithm²⁹ and fourth-order projection methods²⁵ to form a generic fourth-order finite-volume solver for simulating incompressible multiphase flows on moving domains. We also plan to apply this solver to study real-world applications such as wetting and spreading.⁵

Acknowledgment

This work was supported by grants #12272346 and #11871429 from the National Natural Science Foundation of China. The authors acknowledge insightful comments and helpful suggestions from Jiatu Yan and Junxiang Pan, graduate students in the School of Mathematical Sciences at Zhejiang University.

References

1. V. I. Arnold, *Ordinary Differential Equations* (MIT Press, 1973), iISBN: 0-262-51018-9.
2. D. J. Benson, Computational methods in Lagrangian and Eulerian hydrocodes, *Comput. Methods Appl. Mech. Eng.* **99** (1992) 235–394.
3. D. J. Benson, Eulerian finite element methods for the micromechanics of heterogeneous materials: Dynamic prioritization of material interfaces, *Comput. Methods Appl. Mech. Eng.* **151** (1998) 343–360.
4. D. J. Benson, Volume of fluid interface reconstruction methods for multi-material problems, *Appl. Mech. Rev.* **55** (2002) 151–165.
5. D. Bonn, J. Eggers, J. Indekeu, J. Meunier and E. Rolley, Wetting and spreading, *Reviews of Modern Physics* **81** (2009) 739–805.
6. A. Caboussat, M. M. Francois, R. Glowinski, D. B. Kothe and J. M. Sicilian, A numerical method for interface reconstruction of triple points within a volume tracking algorithm, *Mathematical and Computer Modelling* **48** (2008) 1957–1971.
7. B. Y. Choi and M. Bussmann, A piecewise linear approach to volume tracking a triple point, *Int. J. Numer. Meth. Fluids* **53** (2007) 1005–1018.
8. D. de Niem, E. Kührt and U. Motschmann, A volume-of-fluid method for simulation of compressible axisymmetric multi-material flow, *Comput. Phys. Commun.* **176** (2007) 170–190.
9. R. Diestel, *Graph Theory* (Springer, 2017), fifth edition.
10. J. R. Dormand and P. J. Prince, High order embedded Runge-Kutta formulae, *J. Comput. Appl. Math.* **7** (1981) 67–75.
11. V. Dyadechko and M. Shashkov, Reconstruction of multi-material interfaces from moment data, *J. Comput. Phys.* **227** (2008) 5361–5384.
12. P. Hergibo, T. N. Phillips and Z. Xie, A moment-of-fluid method for resolving filamentary structures using a symmetric multi-material approach, *J. Comput. Phys.* **491** (2023) 112401.
13. D. Hu, K. Liang, L. Ying, S. Li and Q. Zhang, ARMS: Adding and removing markers

- on splines for high-order general interface tracking under the MARS framework, *J. Comput. Phys.* **521** (2025) 113574.
14. M. Jemison, M. Sussman and M. Shashkov, Filament capturing with the multimaterial moment-of-fluid method, *J. Comput. Phys.* **285** (2015) 149–172.
 15. M. Kucharik, R. V. Garimella, S. P. Schofield and M. J. Shashkov, A comparative study of interface reconstruction methods for multi-material ALE simulations, *J. Comput. Phys.* **229** (2010) 2432–2452.
 16. S. Mosso and S. Clancy, A geometrically derived priority system for Young’s interface reconstruction, Technical report, Los Alamos National Laboratory, Los Alamos, NM, 1995.
 17. E. G. Puckett, A volume-of-fluid interface tracking algorithm with applications to computing shock wave refraction, in *Proceedings of the Fourth International Symposium on Computational Fluid Dynamics*, ed. H. Dwyer (1991), pp. 933–938.
 18. R. I. Saye and J. A. Sethian, The Voronoi implicit interface method for computing multiphase physics, *PNAS* **108** (2011) 19498–19503.
 19. S. P. Schofield, R. V. Garimella, M. M. Francois and R. Loubère, A second-order accurate material-order-independent interface reconstruction technique for multi-material flow simulations, *J. Comput. Phys.* **228** (2009) 731–745.
 20. C. Sijoy and S. Chaturvedi, Volume-of-fluid algorithm with different modified dynamic material ordering methods and their comparisons, *J. Comput. Phys.* **229** (2010) 3848–3863.
 21. Y. Sui, H. Ding and P. D. Spelt, Numerical simulations of flows with moving contact lines, *Annu. Rev. Fluid Mech.* **46** (2014) 97–119.
 22. L. W. Tu, *An Introduction To Manifolds* (Springer Nature, New York, 2011), 2nd edition.
 23. J. H. Verner, Explicit Runge–Kutta methods with estimates of the local truncation error, *SIAM J. Numer. Anal.* **15** (1978) 772–790.
 24. D. L. Youngs, Time dependent multi-material flow with large fluid distortion, in *Numerical Methods for Fluid Dynamics*, eds. K. W. Morton and M. J. Baines (1982), pp. 273–285.
 25. Q. Zhang, GePUP: Generic projection and unconstrained PPE for fourth-order solutions of the incompressible Navier-Stokes equations with no-slip boundary conditions, *J. Sci. Comput.* **67** (2016) 1134–1180.
 26. Q. Zhang, Fourth-and higher-order interface tracking via mapping and adjusting regular semianalytic sets represented by cubic splines, *SIAM J. Sci. Comput.* **40** (2018) A3755–A3788.
 27. Q. Zhang and A. Fogelson, MARS: An analytic framework of interface tracking via mapping and adjusting regular semialgebraic sets, *SIAM J. Numer. Anal.* **54** (2016) 530–560.
 28. Q. Zhang and Z. Li, Boolean algebra of two-dimensional continua with arbitrarily complex topology, *Math. Comput.* **89** (2020) 2333–2364.
 29. Q. Zhang, Y. Zhu and Z. Li, An AI-aided algorithm for multivariate polynomial reconstruction on Cartesian grids and the PLG finite difference method, *J. Sci. Comput.* **101** (2024) 66.
 30. Q. Zhao, W. Ren and Z. Zhang, A thermodynamically consistent model and its conservative numerical approximation for moving contact lines with soluble surfactants, *Comput. Methods Appl. Mech. Engrg.* **385** (2021) 114033.